

Localisation of Dirac modes in finite-temperature \mathbb{Z}_2 gauge theory on the lattice

György Baranka^a and Matteo Giordano^a

^a*ELTE Eötvös Loránd University, Institute for Theoretical Physics, Pázmány Péter sétány 1/A, H-1117, Budapest, Hungary*

E-mail: barankagy@caesar.elte.hu, giordano@bodri.elte.hu

ABSTRACT: We study the localisation properties of the eigenmodes of the staggered Dirac operator in finite-temperature \mathbb{Z}_2 gauge theory on the lattice in 2+1 dimensions. We find that the low modes turn from delocalised to localised as the system crosses over from the confined to the deconfined phase in the “physical” sector (positive average Polyakov loop), while they remain delocalised in the “unphysical” sector (negative average Polyakov loop). This confirms that the close connection between deconfinement and localisation of the low Dirac modes in the physical sector, already observed in other models, holds also in the simplest gauge theory displaying a deconfinement transition. We also observe a clear correlation of localised modes with fluctuations of the Polyakov loop away from the ordered value, as expected according to the “sea/islands” picture of localisation, and with clusters of negative plaquettes. A novel finding is the presence of localised modes at the high end of the Dirac spectrum in all phases/sectors of the theory.

KEYWORDS: Lattice Quantum Field Theory, Random Systems

Contents

1	Introduction	1
2	\mathbb{Z}_2 lattice gauge theory	4
3	Localisation of Dirac eigenmodes	5
4	Numerical results	9
4.1	Participation ratio	11
4.1.1	Physical sector	12
4.1.2	Unphysical sector	15
4.1.3	Confined phase: both sectors combined	17
4.1.4	Near-zero modes	18
4.2	Spectral density	19
4.3	Correlation of localised modes with gauge observables	20
4.3.1	Polyakov loop	20
4.3.2	Plaquette	22
4.4	Inertia tensor of the eigenmodes	26
5	Conclusions and outlook	33
A	Appendix: IPR for degenerate eigenspaces	35

1 Introduction

In the imaginary-time functional-integral formulation of gauge theories at finite temperature, the effects of dynamical fermions are entirely encoded in the Euclidean Dirac operator in a gauge-field background. The properties of the spectrum of the Euclidean Dirac operator play an important role in various nonperturbative aspects of QCD and other gauge theories, including, e.g., the fate of chiral symmetry [1] and of the $U(1)_A$ anomaly [2–4], and anomalous dimensions in conformal gauge theories [5]. More generally, eigenvalues and eigenvectors of the Euclidean Dirac operator probe the background gauge configuration in a nontrivial way, even in the absence of dynamical fermions.

In recent years it has become apparent that there is a close relation between the localisation properties of the low-lying Dirac modes and the confining properties of gauge theories. It is by now fairly well established, by means of numerical calculations on the lattice, that in the high-temperature phase of QCD the low-lying Dirac modes become localised [6–10]

on the scale of the inverse temperature [7, 9], up to a temperature-dependent point in the spectrum [7]. The same situation is also found in the high-temperature phase of other gauge theories [11–20] and gauge-theory related models [21–25]. This phenomenon has been put into a relation with the ordering of the Polyakov loops in the high-temperature phase [15, 22, 23], or more precisely with the presence of disorder in the form of local fluctuations of the Polyakov loop away from its ordered value. In what has been named the “sea/islands” picture of localisation, the Polyakov loop fluctuations provide “energetically” favourable “islands” for the modes to localise in the middle of a “sea” of ordered Polyakov loops. Numerical evidence of the correlation between localised modes and Polyakov loop fluctuations was presented in Refs. [9, 10, 15].

Localisation of eigenmodes induced by disorder is a well studied phenomenon in condensed matter physics, dating back to the groundbreaking work of Anderson [26]. In the language of condensed matter, disorder leads to the spatial localisation of eigenmodes in certain spectral regions, separated by so-called “mobility edges” from regions where modes are delocalised. Extensive work has led to a thorough understanding of localisation, in particular concerning its aspects at criticality (see, e.g., Refs. [27–30]). Detailed numerical studies have confirmed that localisation of the low-lying Dirac modes in QCD at high temperature T shares the same critical features with three-dimensional Hamiltonians with on-site disorder in the appropriate symmetry class [8, 31, 32]. This provides evidence in support of the conjectured connection between localised modes and Polyakov loop fluctuations, that have the right properties to be the relevant source of disorder.¹

Further insight was obtained in Ref. [23], using an explicit representation of the staggered lattice Dirac operator as a set of coupled Anderson models, with random on-site potential related to the phases of the untraced Polyakov loops. There it was pointed out that besides the presence of disorder in the form of Polyakov loop fluctuations, an important role in the appearance of localised low modes is played by the presence of strong correlations of gauge fields in the temporal direction. Temporal correlations in fact lead to the decoupling of the various Anderson models, and this makes localisation of the low modes possible. While Polyakov loop fluctuations are present also at low T (although there the spatial average of

¹The Dirac operator in finite-temperature QCD belongs to the three-dimensional *chiral* unitary class, but correlation-length critical exponent [8], critical statistics [8, 31] and multifractal exponents [32] match those of the Anderson model in the corresponding *non-chiral* class. A similar result was obtained by Takaishi *et al.* [33] for an Anderson model with correlated, purely off-diagonal disorder in the three-dimensional chiral unitary class, where they found the same critical statistics as in QCD. In a three-dimensional Anderson model with uncorrelated purely off-diagonal logarithmically-distributed disorder in the chiral unitary class, García-García and Cuevas [34] found instead different multifractal exponents than those of the corresponding non-chiral class. However, the model of Ref. [34] requires a much larger amount of off-diagonal disorder than is available in QCD to achieve localisation at the band centre. This suggests that on-site disorder (from the spatial, three-dimensional point of view) is needed to explain localisation of the low modes in QCD, and Polyakov loops match the description. Notice that the universality class of the transition is on the one side not uniquely determined by the symmetry class, and on the other side can be shared by different symmetry classes, see Ref. [29].

the Polyakov loop is close to zero), temporal correlations are induced by the ordering of the Polyakov loops and so are specific to the high- T phase.

Perhaps the most interesting aspect of the sea/islands picture is its simplicity: all that it requires is the presence of order in the Polyakov loop configuration, inducing strong temporal correlations on the one hand, and providing spatially localised fluctuations away from the ordered value on the other. This suggests that all that is required for localised low Dirac modes to appear is the existence of a deconfined phase of the theory, irrespectively of the dimensionality of the system² or the nature of the gauge group. This idea has since been investigated in several models, including pure-gauge SU(3) in 3+1 [17, 19] (see also Refs. [6, 11, 12] for older results) and 2+1 [18] dimensions, a lattice toy model of QCD with unimproved staggered fermions on $N_t = 4$ lattices [16], a QCD-inspired spin model [23, 24], the CP³ model in 2+1 dimensions [25],³ and recently in trace-deformed SU(3) gauge theory in 3+1 dimensions [20]. Results were already available in the case of the SU(2) theory in 3+1 dimensions [14, 35], two-flavour QCD [13] and the Instanton Liquid Model for QCD of Ref. [21]. In all these cases localised low modes have been found in the deconfined phase of the theory. Detailed studies of SU(3) in 3+1 [17, 19] and 2+1 dimensions [18], as well as of the QCD toy model with unimproved fermions [16], the QCD-inspired spin model of Ref. [24], and of trace-deformed SU(3) gauge theory [20], have found convincing evidence that localisation appears precisely at the deconfinement transition. All these findings strongly support the existence of a very close connection between localisation of the low-lying Dirac modes and deconfinement.

The purpose of this work is to push the localisation/deconfinement connection to its limit by studying the simplest lattice gauge theory displaying a finite-temperature deconfining transition: \mathbb{Z}_2 pure gauge theory in 2+1 dimensions [36–38]. This is the simplest possible gauge group, and the lowest dimension where a deconfining transition is found. Furthermore, due to the discrete nature of the gauge group, there are no instanton-related topological aspects of the gauge configurations to take into account, that have been shown to strongly affect the low end of the spectrum in SU(3) gauge theory in 3+1 dimensions [39].

The plan of the paper is the following. In Section 2 we briefly review the relevant aspects of \mathbb{Z}_2 lattice gauge theory. In Section 3 we discuss how to detect localisation of Dirac eigenmodes, and which observables to use in order to study the correlation between localisation and various properties of the gauge field configuration. In Section 4 we show our numerical results. Finally, in Section 5 we present our conclusions and outlook for future studies. Technical details concerning the treatment of degenerate modes are discussed in Appendix A.

²An exception are 1+1 dimensional systems: only localised modes are in fact expected in (spatially) one-dimensional disordered systems, for any amount of disorder (see Refs. [27, 28] and references therein).

³In 1+1 dimensions at finite temperature, localised modes are found in both phases of this model [25], as expected due to the absence of delocalised modes in one-dimensional disordered systems.

2 \mathbb{Z}_2 lattice gauge theory

The dynamical variables of \mathbb{Z}_2 gauge theory on a hypercubic lattice are the link variables $U_\mu(n) = \pm 1$, taking values in \mathbb{Z}_2 , associated to the oriented lattice links connecting site n with its neighbours $n + \hat{\mu}$. In 2+1 dimensions $n = (n_1, n_2, n_3) = (t, \vec{x})$, where $0 \leq t = n_1 \leq N_t - 1$, $0 \leq x_{1,2} = n_{2,3} \leq N_s - 1$, and $\hat{\mu}$ is the unit lattice vector in direction μ , with $\mu = 1, 2, 3$. Periodic boundary conditions are imposed in all directions. The Wilson action for the \mathbb{Z}_2 gauge theory reads (up to an irrelevant additive constant)

$$S[U] = -\beta \sum_n \sum_{\substack{\mu, \nu=1 \\ \mu < \nu}}^3 U_{\mu\nu}(n), \quad (2.1)$$

where the plaquette variables $U_{\mu\nu}$ read simply $U_{\mu\nu}(n) = U_\mu(n)U_\nu(n + \hat{\mu})U_\mu(n + \hat{\nu})U_\nu(n)$, and $\beta = 1/(e^2 a)$ with e the coupling constant (of mass dimension 1/2) and a the lattice spacing. Expectation values are defined as

$$\langle O[U] \rangle = Z^{-1} \sum_{\{U_\mu(n)=\pm 1\}} e^{-S[U]} O[U], \quad Z = \sum_{\{U_\mu(n)=\pm 1\}} e^{-S[U]}, \quad (2.2)$$

where Z is the partition function and the sum is over all possible gauge configurations. The finite-temperature case is studied by taking the thermodynamic limit $N_s \rightarrow \infty$ at fixed N_t , and varying β . In this approach β can be identified with the temperature $T = 1/(aN_t)$ of the system, $T/e^2 = \beta/N_t$.⁴

The phase diagram of the \mathbb{Z}_2 gauge model has been studied in detail in Ref. [40] exploiting the duality relation with the three-dimensional Ising model. A second-order phase transition takes place at a critical $\beta_c = \beta_c(N_t)$, separating a confined phase at $\beta < \beta_c$ from a deconfined one at $\beta > \beta_c$. Deconfinement is signaled by the spontaneous breaking of the centre symmetry of the model, i.e., the symmetry under the transformation

$$U_1(N_t - 1, \vec{x}) \rightarrow z U_1(N_t - 1, \vec{x}) \quad \forall \vec{x}, \quad z \in \mathbb{Z}_2, \quad (2.3)$$

with z an element of the group centre (which for an Abelian group coincides with the group itself). The relevant order parameter is the expectation value, $\langle P(\vec{x}) \rangle$, of the Polyakov loop,

$$P(\vec{x}) \equiv \prod_{t=0}^{N_t-1} U_1(t, \vec{x}). \quad (2.4)$$

In the thermodynamic limit, this vanishes in the confined phase, while it is nonzero in the deconfined phase where the Polyakov loop gets ordered, taking mostly either the +1 or the -1 value. In a finite spatial volume $V = N_s^2$,⁵ we will refer to configurations with positive spatially-averaged Polyakov loop, $\bar{P} \equiv V^{-1} \sum_{\vec{x}} P(\vec{x})$, as belonging to the “physical” sector,

⁴We ignore scaling violations for simplicity.

⁵From now on all quantities are expressed in lattice units, unless explicitly stated otherwise.

and to those with negative \bar{P} as belonging to the “unphysical” sector. The reason for this nomenclature is that when one includes the effects of dynamical fermions via the fermionic determinant, the centre symmetry of the pure-gauge theory is explicitly broken, and the physical sector is expected to be preferred.⁶

In this paper we study the spectrum of the staggered Dirac operator in the background of \mathbb{Z}_2 gauge field configurations. In the case at hand, the staggered operator reads

$$D^{\text{stag}}(n, n') = \frac{1}{2} \sum_{\mu=1}^3 \eta_{\mu}(n) (U_{\mu}(n) \delta_{n+\hat{\mu}, n'} - U_{\mu}(n - \hat{\mu}) \delta_{n-\hat{\mu}, n'}) , \quad \eta_{\mu}(n) = (-1)^{\sum_{\nu < \mu} n_{\nu}} , \quad (2.5)$$

with periodic boundary conditions in the spatial directions and antiperiodic boundary conditions in the temporal direction. The operator D^{stag} is anti-Hermitian and so has purely imaginary eigenvalues,

$$D^{\text{stag}} \psi_l = i \lambda_l \psi_l , \quad \lambda_l \in \mathbb{R} . \quad (2.6)$$

The chiral property $\{\varepsilon, D^{\text{stag}}\} = 0$, with $\varepsilon(n) = (-1)^{\sum_{\mu=1}^3 n_{\mu}}$, implies furthermore

$$D^{\text{stag}} \varepsilon \psi_l = -i \lambda_l \varepsilon \psi_l , \quad (2.7)$$

so that the spectrum is symmetric about zero.

In the continuum limit, D^{stag} describes $N_f = 4$ degenerate species of fermions also in 2+1 dimensions [42].⁷ Here we do not attempt any extrapolation to the continuum limit and work at finite lattice spacing. In this case the staggered fermionic action in the massless limit, $S^{\text{stag}} = \sum_{n, n'} \bar{\chi}(n) D^{\text{stag}}(n, n') \chi(n')$, still retains an exact $U(1)_1 \times U(1)_{\varepsilon}$ chiral symmetry [42] under the following transformations of the fermion fields $\chi, \bar{\chi}$:

$$U(1)_1 : \begin{cases} \chi(n) \rightarrow e^{i\alpha} \chi(n) , \\ \bar{\chi}(n) \rightarrow \bar{\chi}(n) e^{-i\alpha} , \end{cases} \quad U(1)_{\varepsilon} : \begin{cases} \chi(n) \rightarrow e^{i\alpha \varepsilon(n)} \chi(n) , \\ \bar{\chi}(n) \rightarrow \bar{\chi}(n) e^{i\alpha \varepsilon(n)} . \end{cases} \quad (2.8)$$

The $U(1)_{\varepsilon}$ symmetry can break down spontaneously by formation of a quark-antiquark condensate, signalled by a nonzero density of near-zero modes [1]. Although we are working in the opposite, “quenched” limit of infinitely massive fermions, it is nonetheless worth checking whether a nonzero density of near-zero modes is present in the thermodynamic limit.

3 Localisation of Dirac eigenmodes

The simplest way to detect localisation is to study the so-called *inverse participation ratio* (IPR) of the Dirac eigenmodes ψ_l ,

$$\text{IPR}_l \equiv \sum_n |\psi_l(n)|^4 , \quad (3.1)$$

⁶This is known to happen for $SU(2)$ gauge fields, see, e.g., Ref. [41]. We will show that this is the case also for \mathbb{Z}_2 fields when discussing the spectral density of the staggered Dirac operator in Section 4.2.

⁷In Ref. [18] it is mistakenly stated $N_f = 2$.

where it is understood that modes satisfy the normalisation condition $\sum_n |\psi_l(n)|^2 = 1$. Since $|\varepsilon(n)\psi_l(n)| = |\psi_l(n)|$, one finds the same IPR for the eigenmodes corresponding to λ_l and $-\lambda_l$; similar symmetry considerations hold for any observable built out of $|\psi_l(n)|$. It then suffices to consider only $\lambda_l \geq 0$.

For delocalised modes extended throughout the whole lattice, one has the qualitative behaviour $|\psi_{\text{ext}}(n)|^2 \sim (N_t V)^{-1}$, and so $\text{IPR}_{\text{ext}} \sim (N_t V)^{-1}$, which vanishes in the large-volume limit. For modes localised in a region of spatial volume V_0 one has instead approximately $|\psi_{\text{loc}}(n)|^2 \sim (N_t V_0)^{-1}$ within that region and zero outside, and so $\text{IPR}_{\text{loc}} \sim (N_t V_0)^{-1}$, which remains finite as the volume increases. Equivalently, one can consider the *participation ratio* (PR) of the modes,

$$\text{PR}_l \equiv \text{IPR}_l^{-1} (N_t V)^{-1}, \quad (3.2)$$

which measures the fraction of spacetime that they effectively occupy, and as $V \rightarrow \infty$ approaches a constant for extended modes, and zero for localised modes; or the “size” of the modes, $\text{PR}_l \cdot N_t V = \text{IPR}_l^{-1}$, which diverges like V for extended modes, and tends to a constant for localised modes.

To identify the spectral regions where modes are localised, one divides the support of the spectrum in small (ideally infinitesimal) bins, and averages, e.g., the PR of the modes within each bin and over gauge configurations,

$$\text{PR}(\lambda, N_s) \equiv \frac{\langle \sum_l \delta(\lambda - \lambda_l) \text{PR}_l \rangle}{\langle \sum_l \delta(\lambda - \lambda_l) \rangle}, \quad (3.3)$$

studying then the behaviour of $\text{PR}(\lambda, N_s)$ as N_s is changed at fixed λ . In practice, to estimate this quantity locally in the spectrum we divided the full spectral range in bins of small but finite width $\Delta\lambda$, did the averaging within each bin separately, and assigned the result to the average eigenvalue in the bin. The same procedure was used for the other observables considered in this work. At large N_s one expects the following scaling behaviour of $\text{PR}(\lambda, N_s)$,

$$\text{PR}(\lambda, N_s) \simeq c(\lambda) N_s^{\alpha(\lambda)-2}, \quad (3.4)$$

with some volume-indepdent $c(\lambda)$, and where $\alpha(\lambda)$ is the fractal dimension of the eigenmodes in the given spectral region. For extended, fully delocalised modes one has $\alpha = 2$, while for localised modes $\alpha = 0$. The fractal dimension can then be extracted from pairs of different system sizes $N_{s1,2}$ via

$$\alpha(\lambda) = 2 + \log \left(\frac{\text{PR}(\lambda, N_{s1})}{\text{PR}(\lambda, N_{s2})} \right) \bigg/ \log \left(\frac{N_{s1}}{N_{s2}} \right), \quad (3.5)$$

for sufficiently large $N_{s1,2}$.

The presence and the nature of Anderson transitions in two-dimensional systems is a much more delicate issue than in the three-dimensional case. According to the scaling theory of localisation [43], Anderson transitions are generally expected to be absent in two-dimensional disordered systems, and all modes are expected to be localised, except for the

symplectic class (see Refs. [28, 29] for details and references). In practice, however, this issue strongly depends on the details of the system. The inclusion of topological effects in the field-theoretical description of localisation (see Ref. [29] for references) allows the presence of Anderson transitions also in certain other symmetry classes (see Ref. [29] and references cited in Ref. [44]), in particular in the chiral classes [45]. Numerical results show that a second-order Anderson transition is present in the theory of the integer Quantum Hall Effect [46], in the two-dimensional unitary class. An Anderson transition of BKT (Berezinskiĭ-Kosterlitz-Thouless) type is instead present in the two-dimensional unitary Anderson model [44], which is in the same, non-chiral unitary class, and in SU(3) gauge theory in 2+1 dimension [18], which is in the two-dimensional chiral unitary class. An Anderson transition is present also in the CP³ model in 2+1 dimensions [25], again in the two-dimensional chiral unitary class, while for the two-dimensional model with correlated, purely off-diagonal disorder studied in Ref. [33], in the same symmetry class, results are admittedly not conclusive. Finally, a transition of BKT type has been observed also in the orthogonal class, in a model for disordered graphene with strong long-range impurities mimicked by a suitable on-site random potential [47].

The random ‘‘Hamiltonian’’ of interest in this paper is $H = -iD^{\text{stag}}$, which is purely imaginary and satisfies the chiral property $\{\varepsilon, H\} = 0$, and so is invariant under the anti-unitary transformation $T = \eta_5 K$, where K denotes complex conjugation,

$$THT^\dagger = \eta_5 H^* \eta_5 = -\eta_5 H \eta_5 = H. \quad (3.6)$$

Since $T^2 = 1$, H belongs to the chiral orthogonal class [29, 48, 49]. We are not aware of any existing numerical study exploring this case. An argument analogous to that of Refs. [15, 22, 23] shows how local fluctuations of the Polyakov loop effectively provide a two-dimensional on-site disorder. In analogy with what has been found for the SU(3) gauge theory [18], we are then led to expect that if a true Anderson transition is present in the deconfined phase of \mathbb{Z}_2 gauge theory in 2+1 dimensions, then it is of BKT type. This means in particular that we do not expect to find a sudden transition from an ‘‘insulating’’ side (fractal dimension 0) to a ‘‘metallic’’ side (fractal dimension 2) when crossing the mobility edge. All points in the spectrum beyond the mobility edge are in fact expected to be critical, with nontrivial fractal properties of the corresponding eigenmodes, intermediate between insulating and metallic.

It is expected from the sea/islands picture of localisation that localised modes correlate with the fluctuations of the Polyakov loop away from order. To study this correlation we have considered the following observable,

$$\mathcal{P}(\lambda) = \frac{\langle \sum_l \delta(\lambda - \lambda_l) \sum_{t, \vec{x}} P(\vec{x}) |\psi_l(t, \vec{x})|^2 \rangle}{\langle \sum_l \delta(\lambda - \lambda_l) \rangle}, \quad (3.7)$$

i.e., the spatial average of the Polyakov loop weighted by the fermion mode density, or the ‘‘Polyakov loop seen by a mode’’ [15]. For fully delocalised modes one expects

$$\sum_{t, \vec{x}} P(\vec{x}) |\psi_l(t, \vec{x})|^2 \simeq \frac{1}{N_t V} \sum_{t, \vec{x}} P(\vec{x}) = \frac{1}{V} \sum_{\vec{x}} P(\vec{x}) = \bar{P}, \quad (3.8)$$

and so approximately $\mathcal{P} \simeq \langle P \rangle$ in spectral regions where modes are extended. In the physical sector, localised modes are expected to prefer to live close to negative Polyakov loops, and so \mathcal{P} is expected to be considerably smaller than $\langle P \rangle$. Notice that $\frac{1-\mathcal{P}(\lambda)}{2}$ measures exactly “how much” of the mode lives on sites corresponding to a negative Polyakov loop.

The dynamics of the \mathbb{Z}_2 gauge theory can be trivially reexpressed in terms of clusters of negative plaquettes. As pointed out in Ref. [50], what is nontrivial is that at the deconfinement transition (in 2+1 dimensions) the largest such cluster ceases to scale like the system size, i.e., is not fully delocalised. It is then interesting to check whether there is correlation between localised modes and negative plaquettes. To do so we have used two different observables,

$$\mathcal{U}(\lambda) = \frac{\langle \sum_l \delta(\lambda - \lambda_l) \sum_n A(n) |\psi_l(n)|^2 \rangle}{\langle \sum_l \delta(\lambda - \lambda_l) \rangle}, \quad \tilde{\mathcal{U}}(\lambda) = \frac{\langle \sum_l \delta(\lambda - \lambda_l) \sum_{n, A(n) > 0} |\psi_l(n)|^2 \rangle}{\langle \sum_l \delta(\lambda - \lambda_l) \rangle}, \quad (3.9)$$

where $A(n) \geq 0$ counts the number of negative plaquettes touching the lattice site n ,

$$A(n) \equiv \frac{1}{2} \sum_{\substack{\mu, \nu=1 \\ \mu < \nu}}^3 [4 - U_{\mu\nu}(n) - U_{\mu\nu}(n - \hat{\mu}) - U_{\mu\nu}(n - \hat{\nu}) - U_{\mu\nu}(n - \hat{\mu} - \hat{\nu})]. \quad (3.10)$$

$\mathcal{U}(\lambda)$ then measures the average number of negative plaquettes touched by the modes, while $\tilde{\mathcal{U}}(\lambda)$ measures how much of the modes lives on sites touched by negative plaquettes. For delocalised modes one expects

$$\sum_n A(n) |\psi_l(n)|^2 \simeq \frac{1}{N_t V} \sum_n A(n), \quad (3.11)$$

and so approximately $\mathcal{U} \simeq 6(1 - \langle U_{\mu\nu} \rangle)$ in spectral regions where modes are extended. Estimating the probability that $A(n) > 0$, needed to estimate $\tilde{\mathcal{U}}$ for delocalised modes, is instead not so straightforward.

To study the shape of the eigenmodes in more detail we measured their inertia tensor in the centre-of-mass frame, and identified the corresponding principal axes and moments of inertia. A slight complication is due to the fact that the system of interest, i.e., the “mass” distribution $m(n) = |\psi_l(n)|^2$ of mode l , lives on a lattice with periodic boundary conditions, i.e., on a discrete torus. To identify the centre of mass we followed Ref. [51]. Each direction is embedded in a two-dimensional plane as a circle of radius $\frac{N_\mu}{2\pi}$, where N_μ is the linear size in direction μ , with embedding coordinates (ξ_μ, ζ_μ) ,

$$\xi_\mu = N_\mu \cos \theta_\mu(n), \quad \zeta_\mu = N_\mu \sin \theta_\mu(n), \quad \theta_\mu(n) = \frac{2\pi n_\mu}{N_\mu}, \quad 0 \leq n_\mu \leq N_\mu - 1. \quad (3.12)$$

Since $\sum_n m(n) = 1$, the position of the centre-of-mass in the plane is easily found to be

$$\bar{\xi}_\mu = N_\mu \sum_n m(n) \cos \theta_\mu(n), \quad \bar{\zeta}_\mu = N_\mu \sum_n m(n) \sin \theta_\mu(n). \quad (3.13)$$

This is then projected back on the circle via $\bar{\xi}_\mu = \bar{r} \cos \bar{\theta}_\mu$, $\bar{\zeta}_\mu = \bar{r} \sin \bar{\theta}_\mu$, with $\bar{\theta}_\mu \in [0, 2\pi)$ and $\bar{r}^2 = \bar{\xi}_\mu^2 + \bar{\zeta}_\mu^2$. Finally, as long as $\bar{r} \neq 0$, the lattice coordinates of the centre of mass are obtained as

$$\bar{n}_\mu = N_\mu \frac{\bar{\theta}_\mu}{2\pi}. \quad (3.14)$$

If $\bar{r} = 0$, i.e., $\bar{\xi}_\mu = \bar{\zeta}_\mu = 0$, then the mass distribution is uniform in direction μ , and any point can be treated as the centre of mass. The inertia tensor is now defined as

$$\Theta_{\mu\nu} \equiv \sum_n m(n) \left[\left(\sum_\rho (n_\rho - \bar{n}_\rho)^2 \right) \delta_{\mu\nu} - (n_\mu - \bar{n}_\mu)_P (n_\nu - \bar{n}_\nu)_P \right], \quad (3.15)$$

where the periodic coordinate difference $(n_\mu - \bar{n}_\mu)_P$ is defined as⁸

$$(n_\mu - \bar{n}_\mu)_P = \begin{cases} n_\mu - \bar{n}_\mu & \text{if } |n_\mu - \bar{n}_\mu| < |N_\mu - n_\mu + \bar{n}_\mu|, \\ N_\mu - n_\mu + \bar{n}_\mu & \text{if } |n_\mu - \bar{n}_\mu| > |N_\mu - n_\mu + \bar{n}_\mu|. \end{cases} \quad (3.16)$$

From the eigenvalues $\theta_1 \geq \theta_2 \geq \theta_3$ of $\Theta_{\mu\nu}$ one can find out the approximate shape of the mode. There are three particularly interesting cases: i.) $\theta_1 \approx \theta_2 > \theta_3$: the mode is more extended in one direction than in the other two, which are instead approximately equal (elongated, prolate shape); ii.) $\theta_1 > \theta_2 \approx \theta_3$: the mode is less extended in one direction than in the other two, which are instead approximately equal (flattened, oblate shape); iii.) $\theta_1 \approx \theta_2 \approx \theta_3$: the mode is extended approximately in the same way in all directions (spherical shape). Since the temporal direction is singled out, it is also interesting to check the relative orientation of the principal axes of the mode, $v_{1,2,3}$, with the temporal direction. For a randomly oriented axis, one would find for the average of the absolute value of $\cos \varphi_j = v_j \cdot \hat{1}$ the following result,

$$\langle |\cos \varphi_j| \rangle = \frac{1}{2\pi} \int_0^{2\pi} d\phi \int_0^{\frac{\pi}{2}} d\theta \sin \theta \cos \theta = \frac{1}{2}. \quad (3.17)$$

Values larger than 1/2 indicate that the corresponding principal axis prefers to be oriented closer to the temporal direction, while values smaller than 1/2 indicate that it prefers to lie closer to the spatial plane.

4 Numerical results

We performed numerical simulations in both phases of the \mathbb{Z}_2 gauge theory on periodic $N_t \times N_s^2$ cubic lattices with $N_t = 4$ and $N_s = 20, 24, 28, 32$. We used β values in the range $[0.67, 0.77]$ on both sides of the critical coupling, that for $N_t = 4$ is $\beta_c(N_t = 4) = 0.73107(2)$ [40]. Details about the β values and the accumulated statistics can be found in Table 1. Simulations were

⁸Since the centre of mass is almost never located on a lattice site, the case in which one finds equal magnitudes for the coordinate differences obtained following the two possible routes on the torus is very unlikely to happen, and can be ignored. In this case, since neither route is preferred, both should contribute equally to the sum in Eq. (3.15), yielding a vanishing contribution to off-diagonal terms.

N_s	n. of configurations	
	$\beta = 0.67, 0.68, 0.69, 0.70,$ 0.75, 0.76, 0.77	$\beta = 0.71, 0.72, 0.725, 0.73, 0.7325,$ 0.735, 0.7375, 0.74, 0.745
20	2000	4000
24	1000	2000
28	600	1500
32	500	1000

Table 1. Number of configurations (per centre sector) for the various lattice sizes and values of β .

performed with a standard Metropolis algorithm. For each configuration we measured the spatially-averaged Polyakov loop \bar{P} , and depending on its sign we assigned the configuration to the physical sector ($\bar{P} > 0$) or to the unphysical sector ($\bar{P} < 0$). We then obtained a new configuration with the same Boltzmann weight but belonging to the opposite sector by changing the sign of all the temporal links on the last time-slice. Such a configuration was stored separately, leaving the flow of the simulation undisturbed. For both configurations we then obtained all the eigenvalues and eigenvectors of the staggered Dirac operator, Eq. (2.5), using the LAPACK library [52]. We then studied the properties of the eigenmodes locally in the spectrum, dividing the full spectral range in bins of width $\Delta\lambda = 0.05$. Statistical errors were estimated with the jackknife method. The chiral property allowed us to restrict to $\lambda_l \geq 0$ without any loss of information.

Degenerate eigenvalues show up in the spectrum, especially frequently (for some reason unknown to us) in the spectral region around $\lambda_* \equiv \sqrt{3/2}$, which corresponds to the square root of the average squared eigenvalue of the staggered Dirac operator.⁹ This is probably a finite-size effect, as signalled by the fact that the amount of degenerate modes tends to decrease as the lattice size is increased. Nonetheless, it is clearly visible for the lattice sizes studied in this paper. For degenerate eigenspaces it is more appropriate to assign a single value of the IPR to the whole eigenspace. This is obtained by averaging over the eigenspace with the procedure discussed in Appendix A. For observables measuring the correlation of the local density of the modes, $|\psi_l(n)|^2$, with local gauge observables, the result of this averaging procedure coincides with the simple average over any orthonormal basis of the degenerate eigenspace, and no particular treatment is therefore required.

The simplicity of the \mathbb{Z}_2 gauge model allows one to obtain full spectra on lattices of moderately large size. The precise determination of the mobility edge separating regions of delocalised modes from regions of extended modes, on the other hand, requires the use of large system sizes for which full diagonalisation is impractical. In this work we have preferred to obtain an overview of the localisation properties of the modes throughout the whole spectrum, rather than focussing on the low end only, postponing the detailed study of the mobility edge to future work.

⁹In d dimensions, for link variables in an N -dimensional representation of the gauge group (and for $N_t > 2$) one has $-(D^{\text{stag}^2})_{nn} = \frac{d}{2}\mathbf{1}_N$, and so $(N_t V N)^{-1} \sum_l \lambda_l^2 = \frac{d}{2}$.

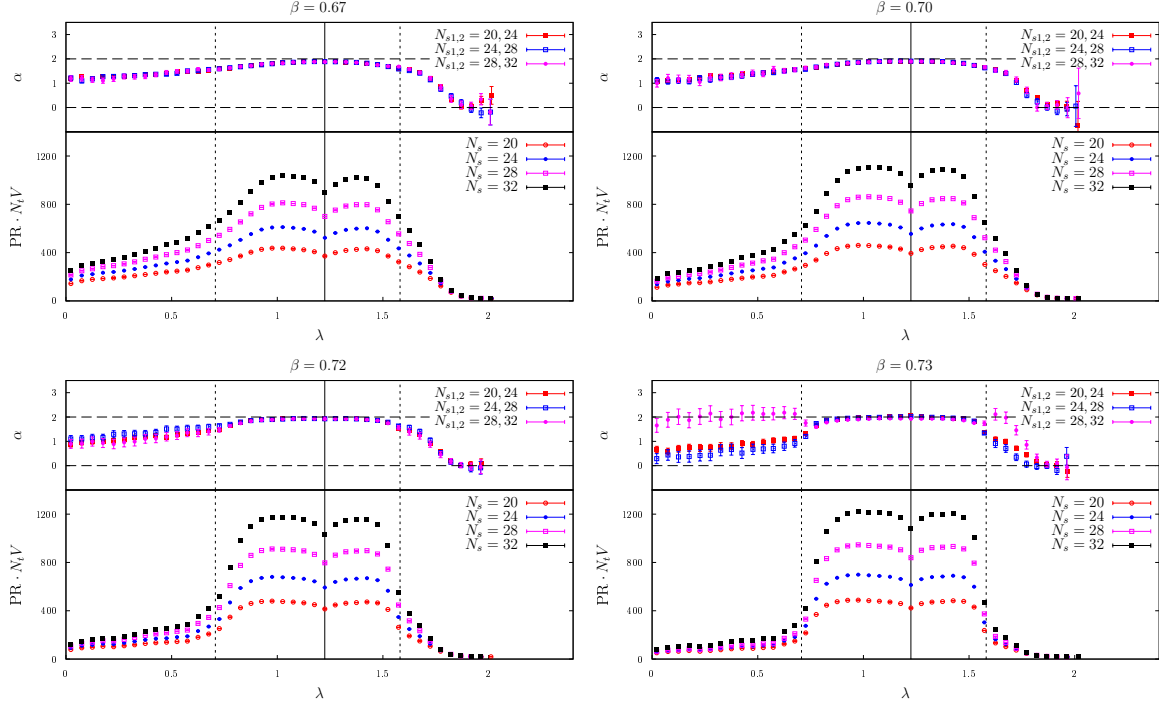


Figure 1. Mode size $\text{PR} \cdot N_t V = \text{IPR}^{-1}$ (bottom) and fractal dimension (top) – confined phase, physical sector. The points $\lambda_{(0)}$, λ_* and $\lambda_{(1)}$ (see Eq. (4.2)) are marked with vertical lines.

For all the observables considered in this paper we have studied the two centre sectors separately. While this corresponds to the two possible choices for the vacuum in the deconfined phase, where centre symmetry is spontaneously broken, in the confined phase the centre symmetry is unbroken and the two sectors should be combined together. Furthermore, in the confined phase the spatially-averaged Polyakov loop, \bar{P} , is small on typical configurations, and one expects little difference between the two sectors. Nevertheless, it is informative to study the two sectors separately, in particular to check how they evolve as the critical coupling is approached.

For couplings close to β_c one expects large finite-size effects for the available lattice sizes, and the corresponding results are therefore not expected to represent accurately the behaviour of the system in the thermodynamic limit. We nonetheless included them in our plots, and they seem qualitatively in line with the general trend.

4.1 Participation ratio

Our numerical results for the “size” of the modes, $\text{PR} \cdot N_t V = \text{IPR}^{-1}$, are shown in Figs. 1, 2 and 3 for the physical sector, and in Figs. 4 and 5 for the unphysical sector, for several values of β both below and above β_c , and for all the available lattice sizes. In the same figures we

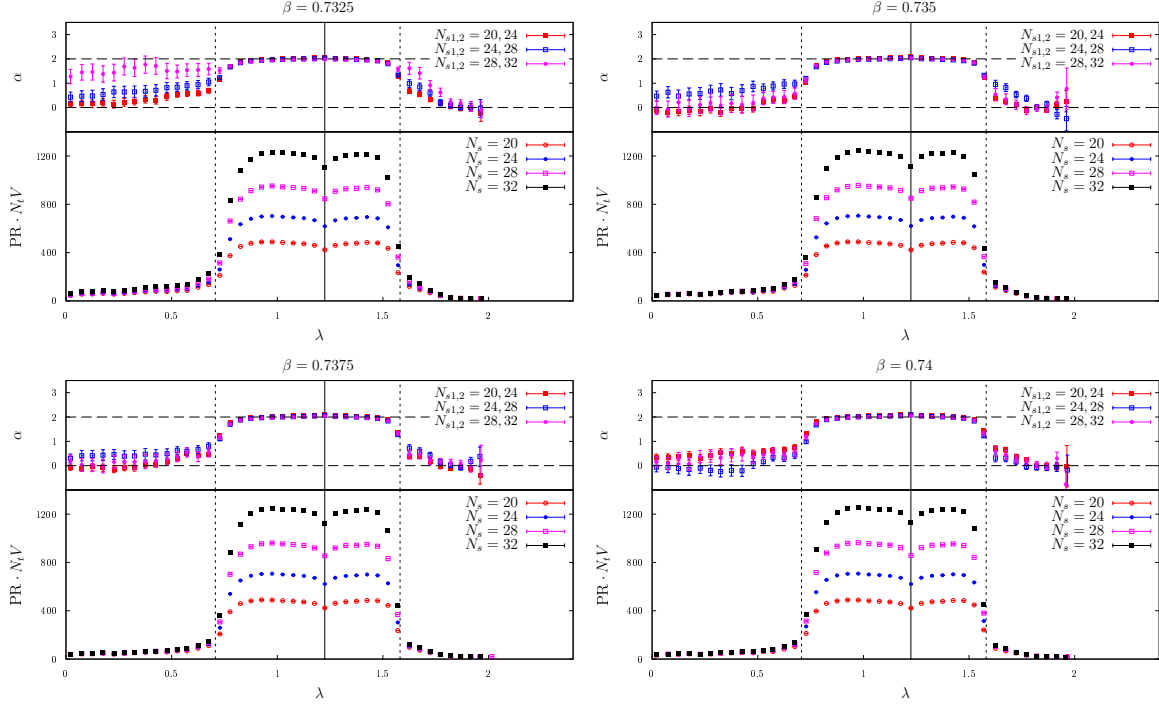


Figure 2. Mode size $\text{PR} \cdot N_t V = \text{IPR}^{-1}$ (bottom) and fractal dimension (top) – deconfined phase, physical sector.

also show the fractal dimension α , computed locally in the spectrum using Eq. (3.5).¹⁰ Its statistical error was estimated by linear propagation of the jackknife errors on $\text{PR}(\lambda, N_s)$.

In the confined phase the contributions of the two centre sectors should be combined to obtain the correct result. This is shown in Fig. 6. We first discuss the results in the two sectors separately, and briefly comment on the combined result in the confined phase afterwards.

4.1.1 Physical sector

The eigenvalues of the free staggered operator (i.e., on the trivial configuration $U_\mu(n) = 1, \forall n, \mu$) in 2+1 dimensions read

$$\lambda_{\text{free}} = \pm \sqrt{(\sin \omega_k)^2 + (\sin p_1)^2 + (\sin p_2)^2}, \quad (4.1)$$

where $\omega_k = \frac{(2k+1)\pi}{N_t}$, $k = 0, \dots, N_t - 1$ are the Matsubara frequencies and $p_j = \frac{2j\pi}{N_s}$, $j = 0, \dots, N_s - 1$ are the lattice momenta. For fixed k , the positive eigenvalues lie in the “Matsubara sector” $[\sin \omega_k, \sqrt{\sin \omega_k^2 + 2}]$,¹¹ and so the whole positive spectrum lies in the interval $[\sin \omega_0, \sqrt{\sin \omega_{\text{max}}^2 + 2}]$, with $\sin \omega_{\text{max}} = \max_k |\sin \omega_k|$. For $N_t = 4$ one has $(\sin \omega_k)^2 = \frac{1}{2} \forall k$.

¹⁰Since the average eigenvalue in the various spectral bins fluctuates slightly for different N_s , it is understood that we compare the average PR in the same spectral bin.

¹¹Here $k = 0, \dots, \frac{N_t}{2} - 1$, while $k = \frac{N_t}{2}, \dots, N_t - 1$ are reserved for the negative spectrum.

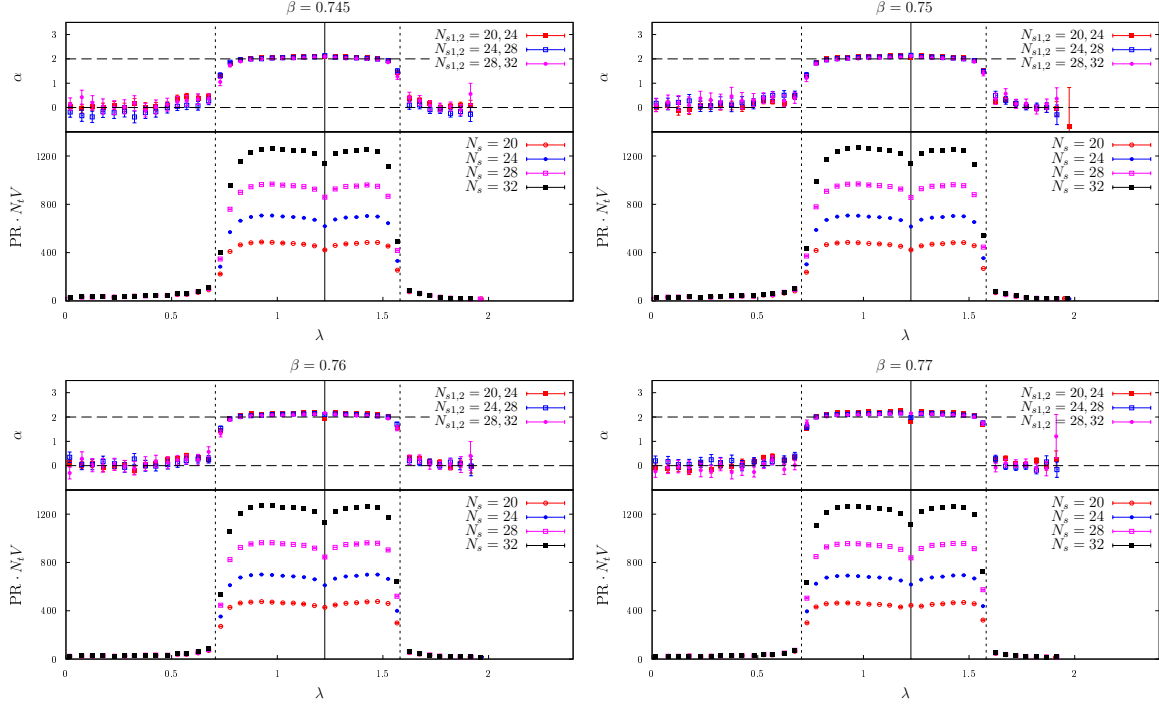


Figure 3. Mode size $\text{PR} \cdot N_t V = \text{IPR}^{-1}$ (bottom) and fractal dimension (top) – deconfined phase, physical sector (continued).

This suggests that one should distinguish three spectral regions in the physical sector: the low modes $\lambda < \lambda_{(0)}$, the bulk modes $\lambda_{(0)} \leq \lambda \leq \lambda_{(1)}$, and the high modes $\lambda > \lambda_{(1)}$, where

$$\lambda_{(0)} \equiv \sin \frac{\pi}{4} = \frac{1}{\sqrt{2}}, \quad \lambda_{(1)} \equiv \sqrt{\left(\sin \frac{\pi}{4}\right)^2 + 2} = \sqrt{\frac{5}{2}}. \quad (4.2)$$

In both phases, the size of the mode, IPR^{-1} , is larger in the bulk than at the edges of the spectrum, as Figs. 1–3 (bottom panel) show. The volume scaling indicates that bulk modes are delocalised in both phases, see Figs. 1–3 (top panel). The low modes, instead, while delocalised in the low-temperature phase, become localised in the high-temperature phase, up to some critical point in the spectrum. More precisely, in the confined phase low modes are delocalised but with a nontrivial fractal dimension, which starting from around $\alpha \approx 1$ for the lowest modes increases towards 2 as one approaches the bulk. In the deconfined phase, instead, for low modes α is close to 0, and starts increasing towards 2 at some point λ_c , which we identify as the mobility edge. While difficult to locate with the current precision, the results shown in Figs. 2 and 3 suggest that $\lambda_c < \lambda_{(0)}$, up to the largest available value of β , and that it increases with β . Finally, the high modes are localised in both phases, above a second mobility edge λ'_c , identified as the point where α , after decreasing from its bulk value, reaches again 0. In this case the results in Figs. 1–3 suggest that $\lambda'_c > \lambda_{(1)}$ up to the largest available value of β . While in the confined phase there seems to be little or no dependence on β , λ'_c seems to decrease with β in the deconfined phase.

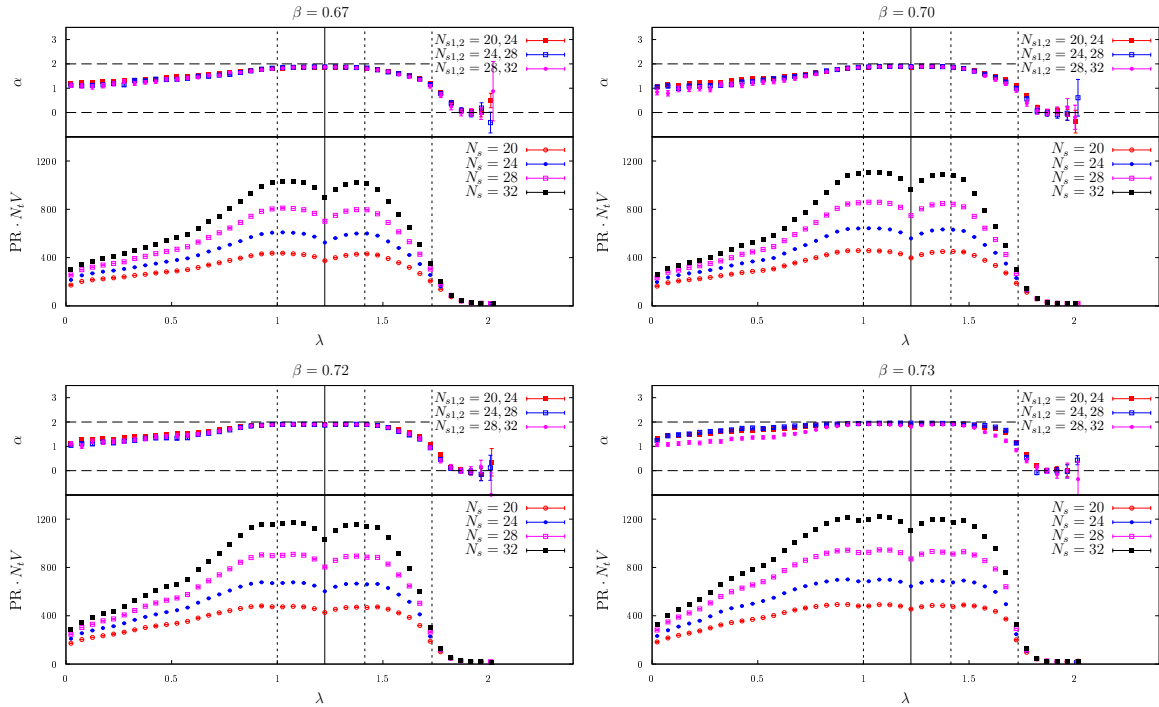


Figure 4. Mode size $\text{PR} \cdot N_t V = \text{IPR}^{-1}$ (bottom) and fractal dimension (top) – confined phase, unphysical sector. The points $\lambda_{(1)}^{\text{PBC}}$, λ_* , $\lambda_{(2)}^{\text{PBC}}$ and $\lambda_{(3)}^{\text{PBC}}$ (see Eq. (4.4)) are marked with vertical lines.

Very large fluctuations in the fractal dimension of the low modes, and of the high modes near $\lambda_{(1)}$, are apparent near β_c . These are a consequence of large finite-size effects, originating from the tunnelling of the system between the two phases, where low modes have different localisation properties. A similar explanation holds for the high modes right above $\lambda_{(1)}$: the second mobility edge, λ'_c , seems in fact independent of β below β_c while it decreases with β above β_c , and tunnelling between the two phases leads to contributions from the “wrong” type of modes. The contribution of these tunnelling configurations are however expected to become negligible as the system size is increased.

Notice that the estimate of the fractal dimension of the bulk modes in the deconfined phase, obtained from the available volumes, sometimes exceeds 2. This is clearly a finite-size effect, indicating that the volume scaling of the bulk modes has not yet reached its asymptotic behaviour (which must be such that $\alpha \leq 2$). This effect is present, and actually stronger, far away from β_c , and is most likely of a different origin than tunneling configurations. A possible explanation is that, as the system grows, not only the effective support of the bulk modes keeps increasing at the same rate, but at the same time these modes become also more uniformly distributed on their support. In any case, our results indicate that α keeps approaching 2 (from above) as the lattice volume grows.

As we mentioned above in Section 3, in the deconfined phase of the present model we do not expect an abrupt change from localised ($\alpha = 0$) to fully delocalised ($\alpha = 2$) modes even

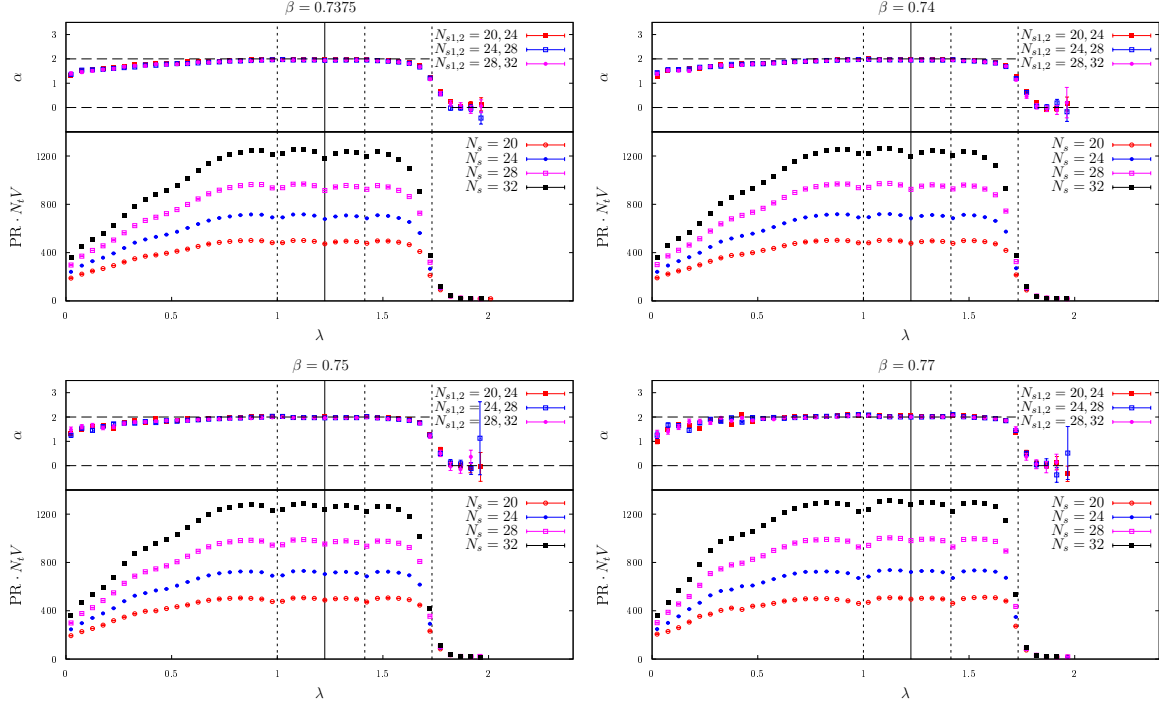


Figure 5. Mode size $\text{PR} \cdot N_t V = \text{IPR}^{-1}$ (bottom) and fractal dimension (top) – deconfined phase, unphysical sector.

in the thermodynamic limit. A spectral range with volume-independent non-trivial fractal dimension seems to be present around $\lambda_{(0)}$, but a detailed study of this issue, as well as the precise location of the mobility edge, is beyond our reach with the available statistics and system sizes. It seems however beyond doubt that the localisation properties of the low modes change across the transition, and the presence of a mobility edge seems very likely.

The clear separation of low, bulk and high modes at high temperature is not surprising. In fact, as β increases the Polyakov loop becomes more and more ordered, inducing stronger and stronger correlations among time slices. This brings the system to fluctuate more and more closely around the trivial configuration, whose Dirac spectrum lies exactly in the range $[\lambda_{(0)}, \lambda_{(1)}]$. It is then not unexpected that modes at both edges of the positive spectrum tend to localise, as they are probably related to the local fluctuations of the gauge configurations away from the trivial one. This will be investigated in detail in the following Subsection. It is interesting to note that also the point λ_* is singled out, with a clear dip in the PR; however, we have no explanation for this behaviour.

4.1.2 Unphysical sector

The analogue of the trivial configuration in the unphysical sector is the gauge configuration with $U_{2,3}(n) = 1 \forall n$, $U_1(n) = 1$ if $n_1 < N_t - 1$, $U_1(n) = -1$ if $n_1 = N_t - 1$. The spectrum of the staggered operator on this configuration is equal to that obtained with the trivial configuration

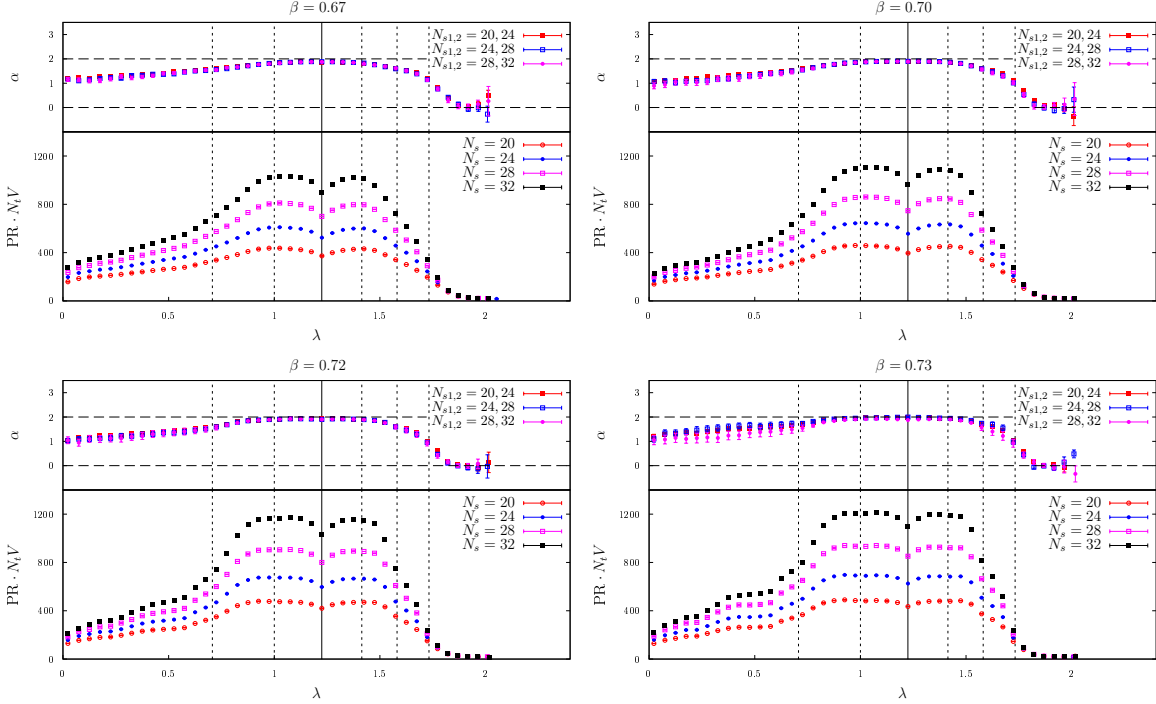


Figure 6. Mode size $\text{PR} \cdot N_t V = \text{IPR}^{-1}$ (bottom) and fractal dimension (top) – confined phase, both sectors combined. The points $\lambda_{(0)}$, $\lambda_{(1)}^{\text{PBC}}$, λ_* , $\lambda_{(2)}^{\text{PBC}}$, $\lambda_{(1)}$ and $\lambda_{(3)}^{\text{PBC}}$ (see Eqs. (4.2) and (4.4)) are marked with vertical lines.

but with temporal boundary conditions switched to periodic instead of antiperiodic,

$$\lambda_{\text{free}}^{\text{PBC}} = \pm \sqrt{(\sin \omega_k^{\text{PBC}})^2 + (\sin p_1)^2 + (\sin p_2)^2}, \quad (4.3)$$

where p_j have been defined under Eq. (4.1), and $\omega_k^{\text{PBC}} = \frac{2k\pi}{N_t}$, $k = 0, \dots, N_t - 1$. For $N_t = 4$ one has $(\sin \omega_{0,2}^{\text{PBC}})^2 = 0$, $(\sin \omega_{1,3}^{\text{PBC}})^2 = 1$. In analogy with the physical sector, one then expects that, at least at high temperature, the points

$$\lambda_{(0)}^{\text{PBC}} \equiv 0, \quad \lambda_{(1)}^{\text{PBC}} \equiv \sin \frac{\pi}{2} = 1, \quad \lambda_{(2)}^{\text{PBC}} \equiv \sqrt{2}, \quad \lambda_{(3)}^{\text{PBC}} \equiv \sqrt{(\sin \frac{\pi}{2})^2 + 2} = \sqrt{3}, \quad (4.4)$$

that correspond to the boundaries of the Matsubara sectors, are singled out in the spectrum. Indeed, as β increases and the system becomes more ordered, one expects the spectrum to resemble more and more the “free” spectrum of Eq. (4.3).

As a matter of fact, in the low-temperature phase the unphysical sector does not differ much from the physical one: as shown in Fig. 4 (bottom panel), all modes are extended, except at the very high end ($\lambda > \lambda_{(3)}^{\text{PBC}}$) where they are localised. In contrast with the physical sector, though, this does not change qualitatively as one crosses over into the high-temperature phase. As it can be seen in Fig. 5 (bottom panel), the tendency is for the mode size to increase everywhere below $\lambda < \lambda_{(3)}^{\text{PBC}}$ (especially below $\lambda_{(1)}^{\text{PBC}}$ and above $\lambda_{(2)}^{\text{PBC}}$), and

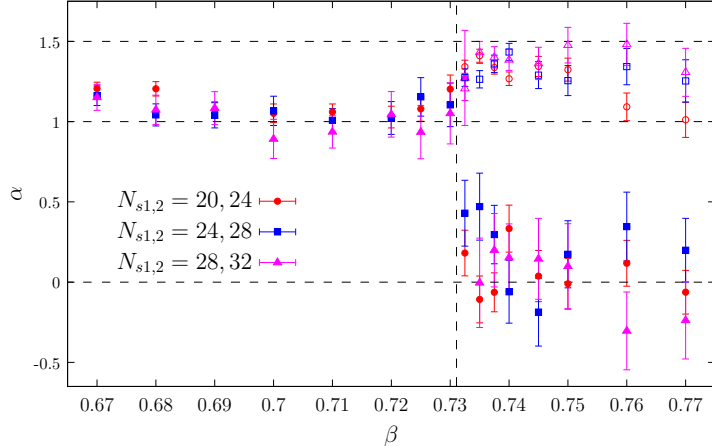


Figure 7. Fractal dimension in the lowest spectral bin, with physical and unphysical sectors combined in the confined phase, and shown separately in the deconfined phase, estimated with various pairs of system sizes. The critical coupling β_c is marked by the dashed vertical line.

to change very little at the high end $\lambda > \lambda_{(3)}^{\text{PBC}}$. Figs. 4 and 5 (bottom panel) suggest that a mobility edge is present at the high end of the spectrum, and that it depends on β very little, or not at all, in both phases of the theory. More detailed information is provided by the fractal dimension, shown in Figs. 4, 5 (top panel). In the confined phase one finds the same situation as in the physical sector, with delocalised low modes with nontrivial fractal dimension $\alpha \approx 1$, delocalised bulk modes with $\alpha \approx 2$, and localised high modes ($\alpha = 0$) above some λ'_c . While no qualitative change is seen when crossing over into the deconfined phase, quantitatively one observes that both the low and bulk modes tend to become more delocalised, with α getting closer to 2 as β increases. Not much seems to change for the high modes above $\lambda_{(3)}^{\text{PBC}}$, with λ'_c barely moving, if at all. As expected, the points $\lambda_{(i)}^{\text{PBC}}$ correspond to features in the PR at high β , as does again the point λ_* : specifically, dips are present at $\lambda_{(1)}^{\text{PBC}}$, $\lambda_{(2)}^{\text{PBC}}$, and λ_* , and the mode size decreases dramatically above $\lambda_{(3)}^{\text{PBC}}$. In contrast with the physical sector, there is no overshooting of the fractal dimension above 2 for the bulk modes, and only near $\lambda_{(1)}^{\text{PBC}}$ and $\lambda_{(2)}^{\text{PBC}}$ one can observe a small effect for the largest β values.

4.1.3 Confined phase: both sectors combined

As already pointed out above, in the confined phase both sectors contribute equally to physical observables. We show the resulting mode size and fractal dimension in Fig. 6. Given the similar behaviour in the two sectors when $\beta < \beta_c$, these plots show little difference from those obtained for the two sectors separately. These plots confirm the presence of localised modes only at the high end of the spectrum, with a mobility edge that shows little to no dependence on β ; and that low modes have a nontrivial fractal dimension.

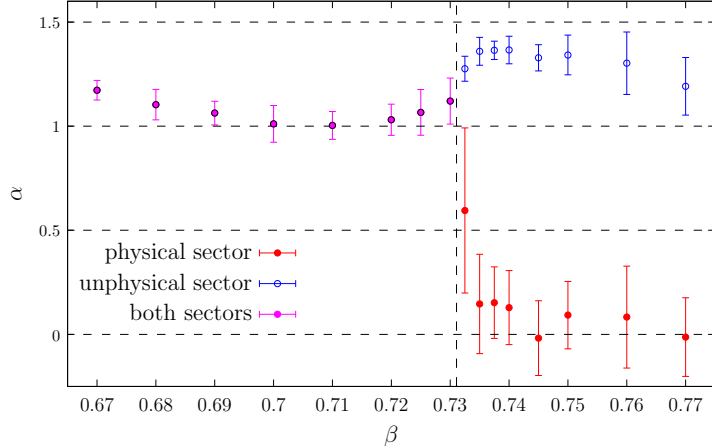


Figure 8. Fractal dimension in the lowest spectral bin, estimated by averaging over all pairs of system sizes with $20 \leq N_s \leq 32$. The two centre sectors are combined for $\beta < \beta_c$, and shown separately for $\beta > \beta_c$, with β_c marked by the dashed vertical line.

4.1.4 Near-zero modes

In order to summarise the dependence on temperature of the localisation properties of the low modes, in Figs. 7 and 8 we show the fractal dimension of modes in the lowest spectral bin, as a function of β . More precisely, in Fig. 7 we show estimates of the fractal dimension obtained from several pairs of volumes, treating the two centre sectors together in the confined phase, and separately in the deconfined phase. For $\beta < \beta_c$, α tends to slightly decrease as β increases, from slightly above 1 towards 1 up to around β_c . Above β_c it drops towards 0, in the physical sector, and increases to approximately $1.2 \div 1.4$, in the unphysical sector. Finite-size effects are small at low β , expectedly large around β_c , and again reasonably small above β_c , although larger than in the low-temperature phase. In Fig. 8 we show an estimate of the fractal dimension α of the lowest modes obtained after averaging over all pairs of available system sizes. Error bars correspond to the sum in quadrature of the average statistical error and of the finite-size systematic error, estimated as the variance of α over the pairs of N_s values. Our results show clearly that the two centre sectors respond very differently to the phase transition, with low modes becoming more delocalised in the unphysical sector, and localised in the physical sector.

Although the use of only moderately large volumes, for which large finite-size effects are still present near β_c , does not allow us to make a conclusive statement, it seems likely that in the thermodynamic limit an abrupt transition from $\alpha \approx 1$ to $\alpha = 0$ will take place at β_c in the physical sector. Conclusive evidence requires the extension of the present study to larger system sizes.

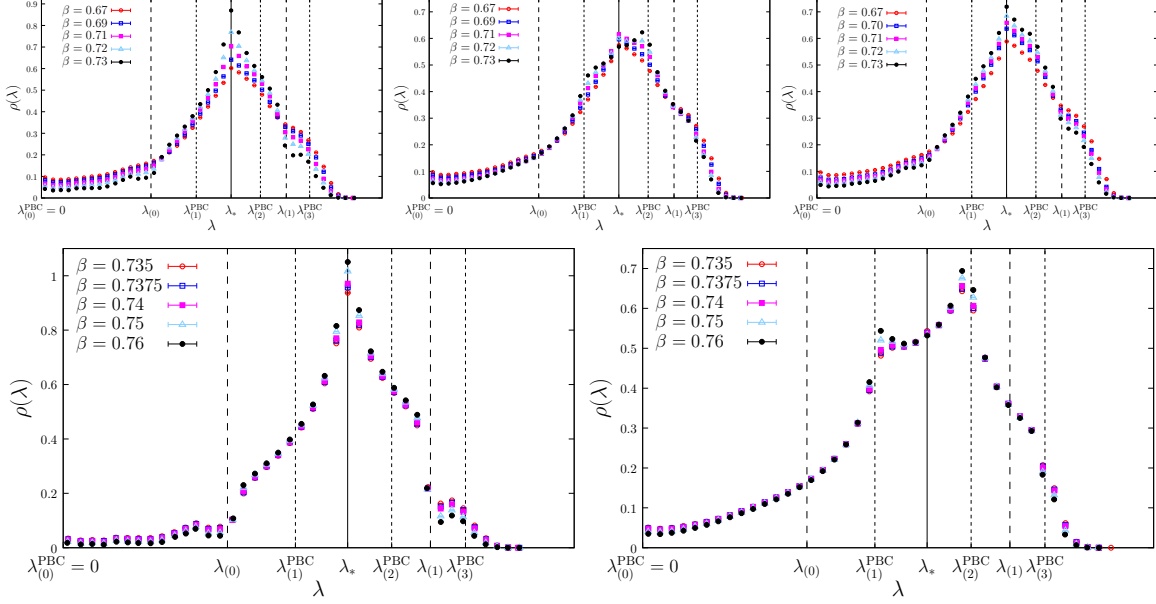


Figure 9. Spectral density – confined phase, physical (top left) and unphysical (top center) sector, and both sectors together (top right); deconfined phase, physical (bottom left) and unphysical (bottom right) sector. Here $N_s = 32$.

4.2 Spectral density

The spectral density per unit lattice volume, ρ ,

$$\rho(\lambda) \equiv (N_t V)^{-1} \langle \sum_l \delta(\lambda - \lambda_l) \rangle, \quad (4.5)$$

is shown in Fig. 9 for several values of β , for the physical and unphysical sectors separately, and for both sectors together in the confined phase. The dependence on the system size is negligible, so only the largest size $N_s = 32$ is shown. The points $\lambda_{(i)}$, $i = 0, 1, 2$ and $\lambda_{(i)}^{\text{PBC}}$, $i = 0, 1, 2, 3$, as well as λ_* , are marked. The spectral density is large in the bulk and small at the low and high end; remarkably, it does not vanish at the low end $\lambda \simeq 0$ in either phase. The spectral density $\rho(0^+)$ in the lowest bin $[0, \Delta\lambda]$ is shown in Fig. 10, again for $N_s = 32$, for the two centre sectors separately and for both sectors combined (also in the deconfined phase for comparison). While $\rho(0^+)$ keeps decreasing with β , it remains nonzero in both sectors up to the largest β studied here. Loosely speaking, this indicates chiral symmetry breaking by a (valence) quark-antiquark condensate both in the confined and in the deconfined phase of the theory. Furthermore, comparing the physically meaningful results, i.e., both sectors added up in the confined phase and treated separately in the deconfined phase, one sees that $\rho(0^+)$ jumps at β_c , downwards (resp. upwards) if the physical (resp. unphysical) sector is chosen in the deconfined phase.¹² This means that while chiral symmetry remains broken in the high- β

¹²Notice that since the spectral density near zero is smaller in the physical sector, this sector will be favoured in the presence of dynamical fermions.

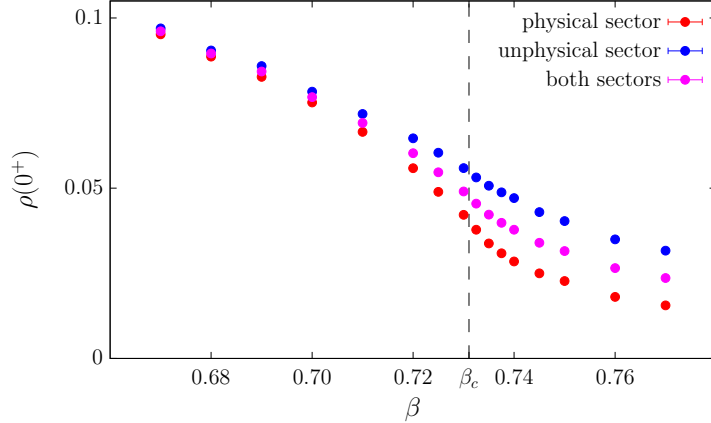


Figure 10. Spectral density of near-zero modes. The case of the two centre sectors combined in the deconfined phase is shown only for comparison. Here $N_s = 32$.

phase, a first-order phase transition is displayed also in the chiral properties. Moreover, in the physical sector in the deconfined phase the low modes are localised. A similar situation is found in $SU(3)$ pure-gauge theory in 3+1 dimensions [17, 19], where however the near-zero localised modes stand out as a prominent peak, rather than being part of a plateau as in the present case. The inclusion of dynamical fermions is expected to lower the density of near-zero modes, but it is possible that even in this case the \mathbb{Z}_2 theory displays a first-order transition to a phase with a non-zero density of localised near-zero modes. If this scenario survived also in the chiral limit (taken after the continuum limit, also assumed to exist), it would lead to the disappearance of the massless Goldstone modes associated with the spontaneous breaking of the $SU(N_f = 4)_A$ symmetry of the theory [53].

A curious feature is the presence of a peak at λ_* at all β in the physical sector, and at low $\beta < \beta_c$ in the unphysical sector. At high $\beta > \beta_c$ in the unphysical sector this peak disappears, and is replaced by two peaks near $\lambda_{(1)}^{(\text{PBC})}$ and $\lambda_{(2)}^{(\text{PBC})}$. We do not know the reason behind these peaks and the analogous presence of features at λ_* (as well as at $\lambda_{(i)}$ or $\lambda_{(i)}^{(\text{PBC})}$) in most observables considered in this work.

4.3 Correlation of localised modes with gauge observables

4.3.1 Polyakov loop

According to the sea/islands picture of localisation [15, 22, 23], localised modes in the physical sector of the deconfined phase are expected to live near fluctuations of the Polyakov loop away from the ordered value. For \mathbb{Z}_2 the Polyakov loop can take only two values, and we expect the localised modes to prefer sites where $P(\vec{x}) = -1$. In Figs. 11 and 12 we show the Polyakov loop weighted by the eigenmodes $\mathcal{P}(\lambda)$, Eq. (3.7), for the physical (top panel) and unphysical (bottom panel) sectors.

Let us discuss first the physical sector. In the confined phase, while delocalised, the low modes show a moderate but clear preference for negative Polyakov loops; the bulk modes

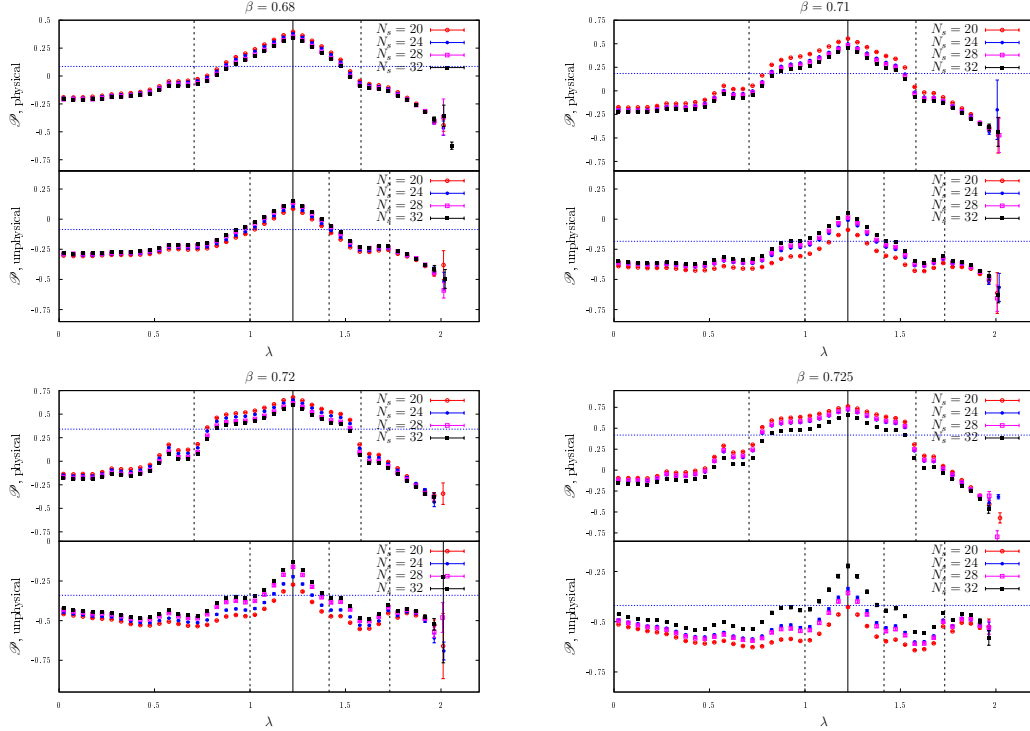


Figure 11. Polyakov loop weighted by the modes – confined phase, physical (top) and unphysical (bottom) sectors. Here and in the following plot, the horizontal lines corresponds to $\pm \langle |\bar{P}| \rangle$ on the largest available volume ($N_s = 32$).

show a moderate but clear preference for positive Polyakov loops, with \mathcal{P} above the average of \bar{P} in the physical sector,¹³ and the high modes, which are localised, show a clear preference for negative Polyakov loops. Throughout the spectrum, $\mathcal{P}(\lambda)$ decreases slightly with the volume, probably reflecting the fact that $\langle |\bar{P}| \rangle \rightarrow 0$ in the thermodynamic limit; it seems likely though that a nontrivial $\mathcal{P}(\lambda)$ will be found also in this limit. In the deconfined phase the low modes, which are now localised, have roughly half of their weight on sites with positive Polyakov loop and half on the now much rarer sites with negative Polyakov loop. This is in agreement with expectations. More precisely, the ratio between the average number of sites with negative Polyakov loop “occupied” by a mode and the average number of sites with negative Polyakov loop, i.e., $(1 - \mathcal{P}(\lambda))/(1 - \langle |\bar{P}| \rangle)$, increases steadily with β in the deconfined phase. Bulk modes tend instead to avoid negative Polyakov loops, as shown by the fact that $1 - \mathcal{P}(\lambda) < 1 - \langle |\bar{P}| \rangle$. High modes are again clearly preferring negative Polyakov loops, with more than half of the mode’s weight concentrated on the corresponding sites. In the deconfined phase the dependence of \mathcal{P} on the volume seems very mild.

We now discuss the unphysical sector. In the confined phase, negative Polyakov loops

¹³By construction, the average of \bar{P} in the two centre sectors is simply $\pm \langle |\bar{P}| \rangle$, where the average is over the ensemble of configurations generated in the Monte-Carlo simulation.

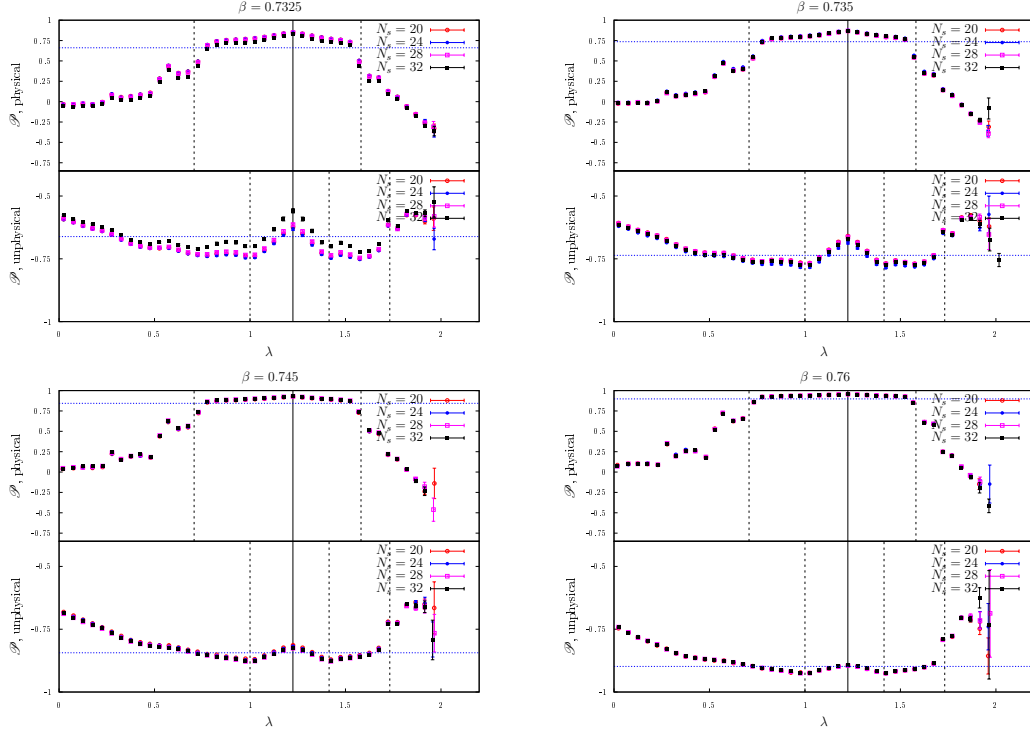


Figure 12. Polyakov loop weighted by the modes – deconfined phase, physical (top) and unphysical (bottom) sectors.

seem again to be preferred everywhere in the spectrum except in the very middle, where positive Polyakov loops are slightly preferred. In fact, also in this case $\mathcal{P}(\lambda)$ for the bulk modes is above the average of \bar{P} in the given centre sector, although in this case it means that they favour the slightly less frequent positive loops to the negative ones (in the physical sector they prefer instead the more frequent positive loops). Low and high modes instead have $\mathcal{P}(\lambda) < -\langle |\bar{P}| \rangle$. The tendency is this time for $\mathcal{P}(\lambda)$ to increase as the volume increases. In the deconfined phase $\mathcal{P}(\lambda)$ becomes flatter in the bulk, where $\mathcal{P}(\lambda)$ gets closer to $-\langle |\bar{P}| \rangle$, while low and high modes show now clearly $0 > \mathcal{P}(\lambda) > -\langle |\bar{P}| \rangle$, thus favouring positive Polyakov loops; the volume dependence is again very mild. The correlation of low modes with positive Polyakov loops in the deconfined phase cannot be simply explained in terms of “energetically” favourable islands “attracting” the mode. It is however not in contrast with the sea/islands picture of localisation. We elaborate on this point in the conclusions.

4.3.2 Plaquette

We now turn to the correlation between localised modes and negative plaquettes, for which we provide two different measures. In Figs. 13 and 14 we show $\mathcal{U}(\lambda)$, which measures the average number of negative plaquettes touched by the modes (see Eq. (3.9)) or, equivalently, the “negative plaquettes seen by the modes”. In Figs. 15 and 16 we show instead $\tilde{\mathcal{U}}(\lambda)$,

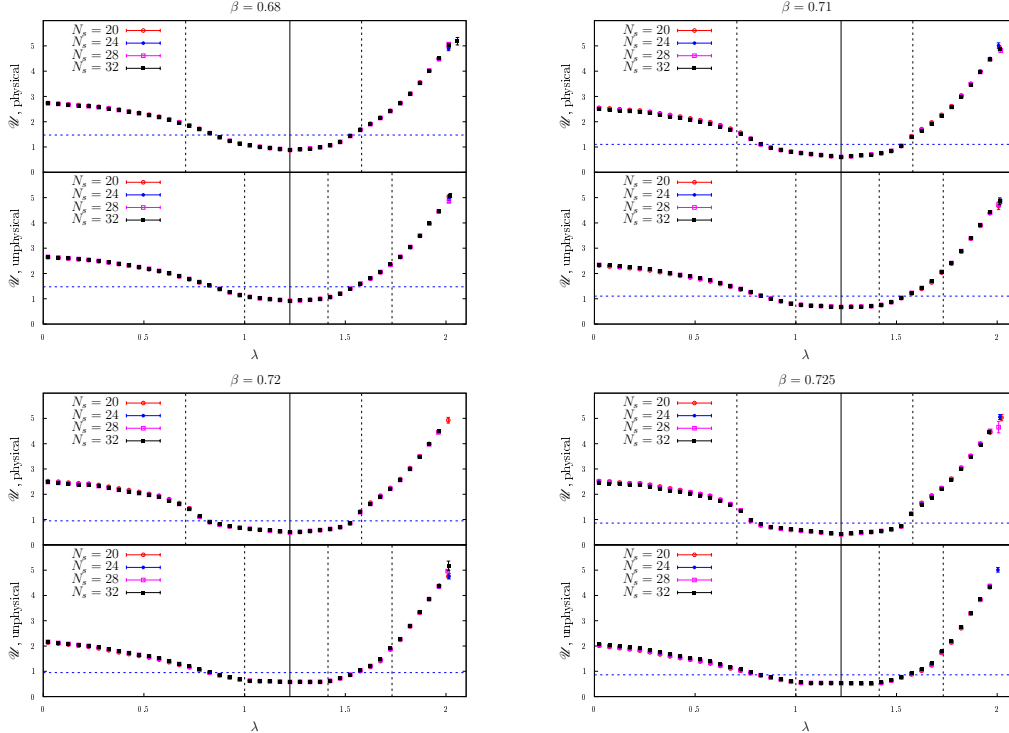


Figure 13. Average number of negative plaquettes touched by a mode – confined phase, physical (top) and unphysical (bottom) sectors. Here and in the following plots, the horizontal line corresponds to $6\langle 1 - U_{\mu\nu} \rangle$ on the largest available volume ($N_s = 32$).

which measures what fraction of the modes lives on sites touched by at least one negative plaquette (see Eq. (3.9)). The two observables provide slightly different information: $\tilde{\mathcal{W}}(\lambda)$ tells us “how much” of the modes lives near negative plaquettes, while $\mathcal{W}(\lambda)$ tells us how much of the modes like to live near *clusters* of negative plaquettes.

We discuss $\mathcal{W}(\lambda)$ first. In the physical sector (Figs. 13 and 14, top panel) the low and high modes prefer to be closer to negative plaquettes ($\mathcal{W}(\lambda) > 6\langle 1 - U_{\mu\nu} \rangle$), while bulk modes prefer to avoid them ($\mathcal{W}(\lambda) < 6\langle 1 - U_{\mu\nu} \rangle$), in both phases of the theory. More precisely, the low and, especially, the high modes have a larger weight on sites touching more than one negative plaquette, and so prefer to live close to where negative plaquettes tend to cluster. No clear dependence on the volume is visible. $\mathcal{W}(\lambda)$ shows little dependence on β as well, the only notable features being that for bulk modes the tendency to avoid negative plaquettes is much less pronounced in the deconfined phase, where $\mathcal{W}(\lambda)$ also becomes flatter. For the high modes $\mathcal{W}(\lambda)$ changes very little with β ; for the low modes it slightly decreases as the deconfined phase is approached, remaining essentially constant in the deconfined phase. Since the average number of negative plaquettes decreases as β is increased, this means that the localised low and high modes are more and more localised near clusters of negative plaquettes as one gets deeper in the deconfined phase.

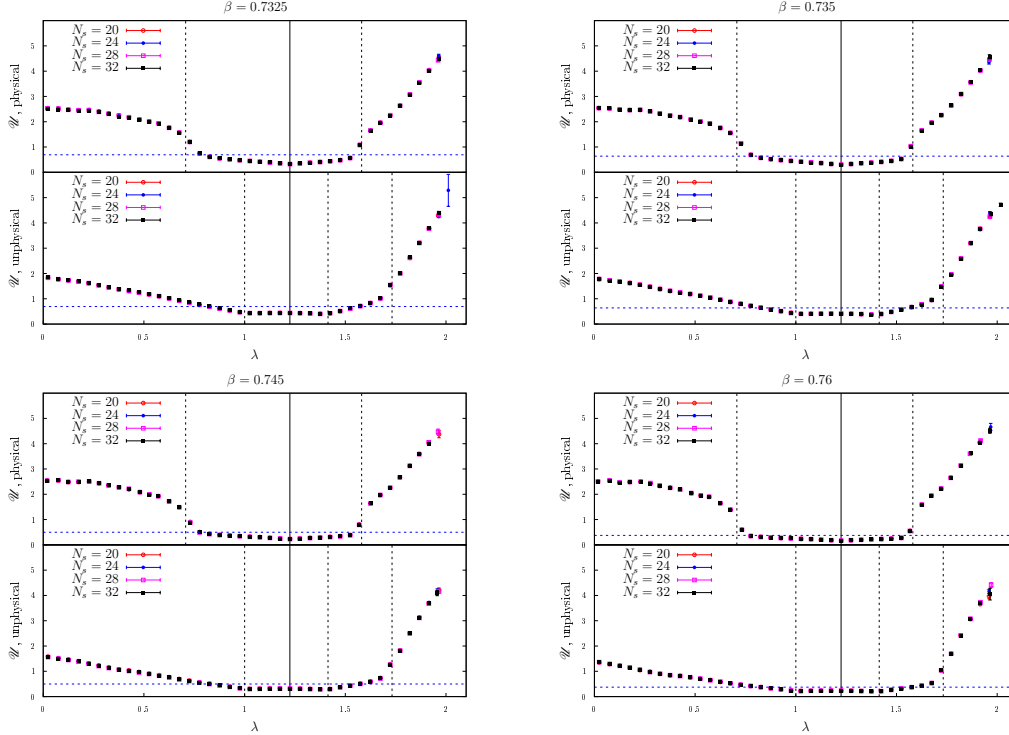


Figure 14. Average number of negative plaquettes touched by a mode – deconfined phase, physical (top) and unphysical (bottom) sectors.

The situation is quite similar in the unphysical sector (Figs. 13 and 14, bottom panel): low and high modes still prefer to be near clusters of negative plaquettes, and bulk modes prefer to avoid them. Again, no clear volume dependence is visible. The dependence on β is slightly stronger than in the physical sector: here not only $\mathcal{U}(\lambda)$ for bulk modes becomes flatter and closer to $6\langle 1 - U_{\mu\nu} \rangle$ as β increases, but also the upward deviation of $\mathcal{U}(\lambda)$ from $6\langle 1 - U_{\mu\nu} \rangle$ for low modes becomes less pronounced. As low and bulk modes are delocalised, this is in line with the fact that negative plaquettes become less frequent in the deconfined phase. For the localised high modes the change of $\mathcal{U}(\lambda)$ with β is small, indicating again that they prefer to localise more near negative plaquettes as β increases.

We now turn to $\tilde{\mathcal{W}}(\lambda)$. In the physical sector (Figs. 15 and 16, top panel), and for all β , 80% or more of the weight of low and high modes is on sites touching at least one negative plaquette, while for bulk modes this fraction is 80% or less, and decreasing rapidly as one approaches λ_* from either side. For low and high modes there seems to be little variation as β increases, despite the fact that negative plaquettes become rarer, while for bulk modes $\tilde{\mathcal{W}}(\lambda)$ clearly decreases with β . This again indicates that localised modes tend to localise near negative plaquettes. In the unphysical sector (Figs. 15 and 16, bottom panel), low and high modes have again a much larger value of $\tilde{\mathcal{W}}(\lambda)$ than bulk modes at all β s. Differently from the physical sector, $\tilde{\mathcal{W}}(\lambda)$ clearly decreases as β increases both for low and bulk modes, while

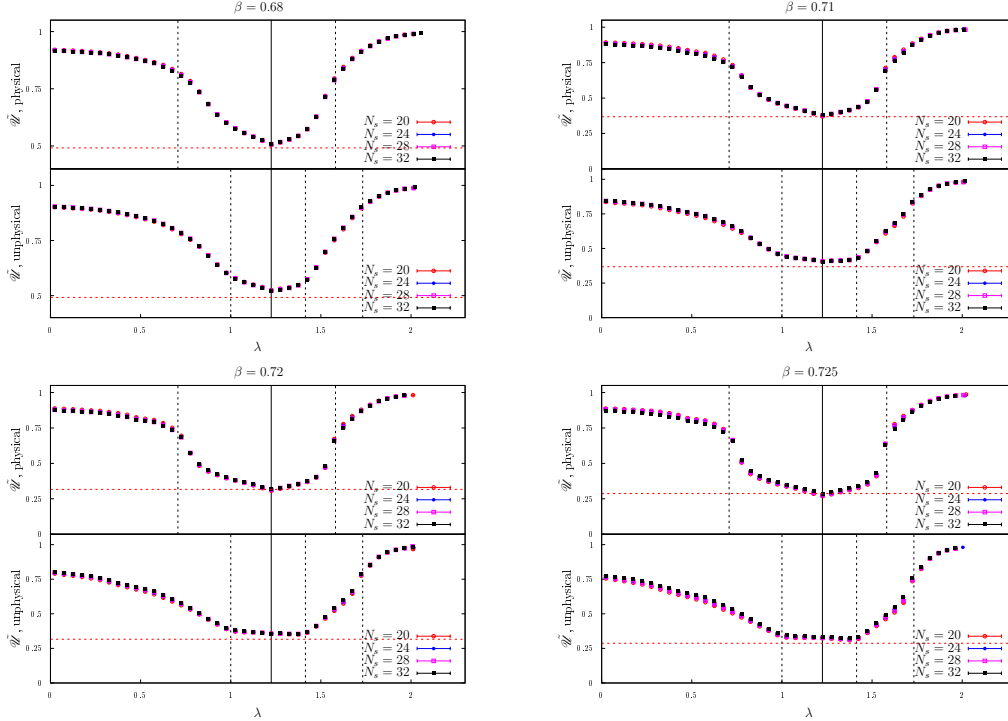


Figure 15. Fraction of mode touched by negative plaquettes – confined phase, physical (top) and unphysical (bottom) sectors. Here and in the following plots, the horizontal line corresponds to $2(1 - \langle U_{\mu\nu} \rangle)$ on the largest available volume ($N_s = 32$).

for high modes it shows very little dependence on β . This again indicates that the localised high modes prefer to localise near negative plaquettes. As already mentioned in Section 3, it is not straightforward to estimate what one should expect for $\mathcal{W}(\lambda)$ in the case of fully delocalised modes ($|\psi|^2 \sim 1/(N_t V)$). It turns out that $2(1 - \langle U_{\mu\nu} \rangle)$ provides an accurate lower bound on $\mathcal{W}(\lambda)$ in the bulk of the spectrum.

The stronger correlation between localised modes and negative plaquettes than between localised modes and Polyakov loop fluctuations does not necessarily mean that the former are better candidates as the relevant source of disorder than the latter. On the one hand, negative plaquettes are strongly correlated with Polyakov loop fluctuations. On the other hand, localised modes in the deconfined phase, physical sector, are not strictly confined to Polyakov loop fluctuations away from the ordered value, as that would be “energetically” expensive. One can then reconcile the observed stronger correlation with negative plaquettes and the Polyakov loop fluctuations being the actual source of disorder, if localisation takes place on clusters of negative plaquettes near the Polyakov loop fluctuations. This is particularly interesting in the light of the observation [50] that the largest negative-plaquette cluster scales as the system size in the confined phase, while it remains finite in the deconfined phase. This may help explain the relation between deconfinement and localisation (and between confinement and delocalisation) of the low modes in the physical sector. This point deserves a more

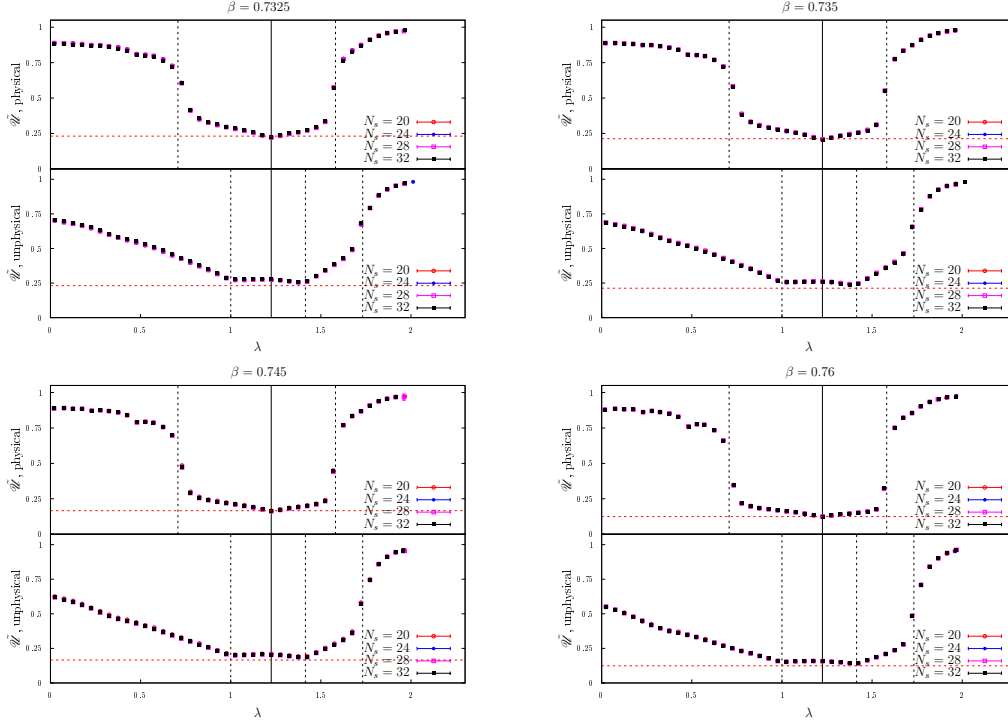


Figure 16. Fraction of mode touched by negative plaquettes – deconfined phase, physical (top) and unphysical (bottom) sectors.

detailed study, which is however outside of the scope of the present paper.

4.4 Inertia tensor of the eigenmodes

The inertia tensor of the eigenmodes is expected not only to distinguish between localised and delocalised modes, but also to provide more detailed information on their shape. In order to interpret the numerical results, we model the eigenmodes as homogeneous cuboids of unit mass, of length ℓ_i in direction v_i , with $\{v_{1,2,3}\}$ the orthonormal set of eigenvectors of the inertia tensor, i.e., the principal axes of the mode. For such a cuboid, the principal moment of inertia θ_1 corresponding to v_1 is $\theta_1^{\text{cont}} = \frac{1}{12}(\ell_2^2 + \ell_3^2)$ for a continuous mass distribution, and $\theta_1^{\text{lat}} = \frac{1}{12}(\ell_2^2 + \ell_3^2 - 2)$ on a periodic lattice; similar expressions hold for the other two principal moments. From these expressions one easily recovers the length of the sides of the equivalent cuboid with the same principal moments as the given eigenmode. Alternatively, one can model the eigenmodes as ellipsoids, which is perhaps more appropriate for localised modes. One would then find for θ_1 the following expression in terms of the axes length ℓ'_i (for a continuous mass distribution), $\theta_1^{\text{cont}} = \frac{1}{20}(\ell_2'^2 + \ell_3'^2)$, and similar expressions for the other moments.

The volume scaling $\theta_i \sim N_s^{\tilde{\alpha}_i}$ of the principal moments should reflect the localised ($\tilde{\alpha}_i = 0$) or delocalised ($\tilde{\alpha}_i = 2$) nature of the modes. In fact, both in the cuboid and in the ellipsoid description, at least one of the two contributions to any of the principal moments should scale

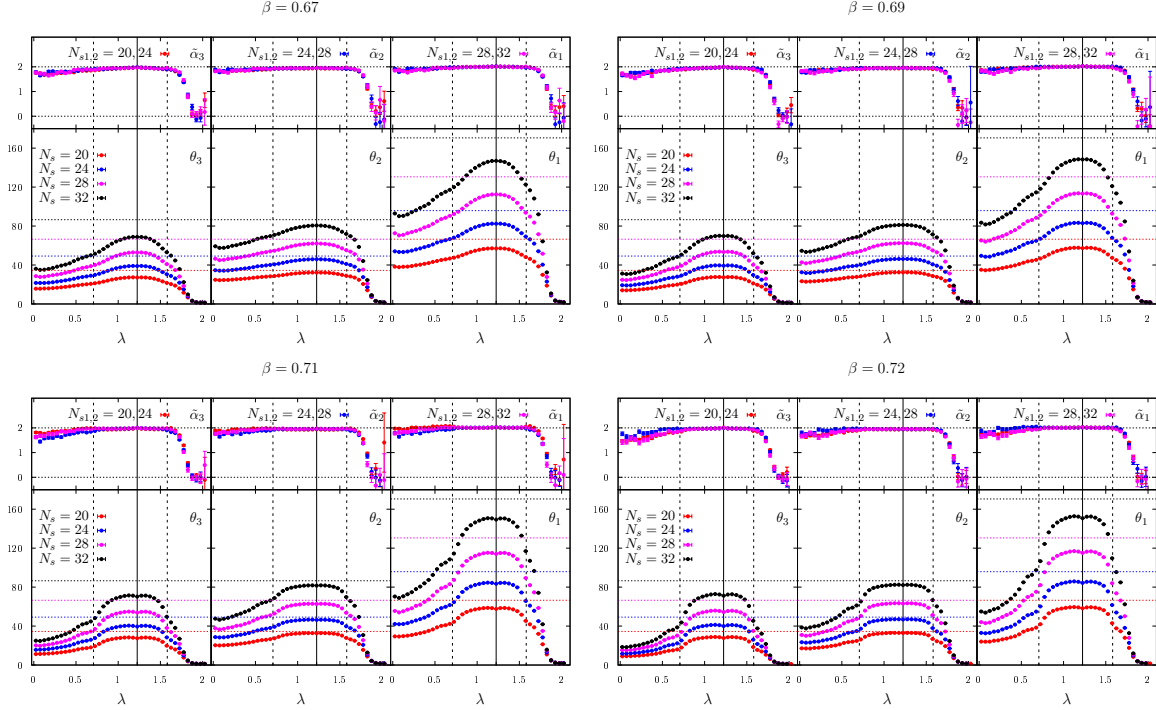


Figure 17. Bottom panels: average principal moments of inertia θ_i – confined phase, physical sector. The expectation for a cuboid of size $N_t \times N_s \times N_s$ is also shown (colour code matching that of the numerical data for the various volumes). Top panels: scaling dimension $\tilde{\alpha}_i$ of moment θ_i for various pairs of volumes.

like N_s^2 for a spatially delocalised mode, while they should all remain finite as N_s grows for a spatially localised mode.

Concerning the shape of the eigenmode, interesting cases are $\theta_1 \approx \theta_2 > \theta_3$, corresponding to a “rod-like” shape, or prolate spheroid, depending on how one models the modes; $\theta_1 > \theta_2 \approx \theta_3$, corresponding to a “slab-like” shape, or oblate spheroid; and $\theta_1 \approx \theta_2 \approx \theta_3$, corresponding to a cube or sphere. As a measure of isotropy/sphericity, one can use $\frac{1}{2} \log \frac{\theta_1}{\theta_3}$: the closer to zero, the more spherical the mode. Depending on its sign, the quantity $\log \frac{\theta_2}{\theta_3} - \frac{1}{2} \log \frac{\theta_1}{\theta_3} = \frac{1}{2} \log \frac{\theta_2^2}{\theta_1 \theta_3}$ provides instead a measure of prolateness (if < 0) or oblateness (if > 0) of the modes.

Finally, from the principal axes one can determine the typical orientation of the eigenmodes with respect to the temporal direction. For delocalised modes extended throughout the lattice, one expects one axis along the temporal direction and two lying in the spatial plane. For localised modes one can further distinguish between modes extended in the temporal direction, and modes localised in the temporal direction (possibly on a comparable scale). In the first case one similarly expects one principal axis along the temporal direction and two in the spatial plane, while in the second case the orientation of the mode with respect to the temporal direction can fluctuate.

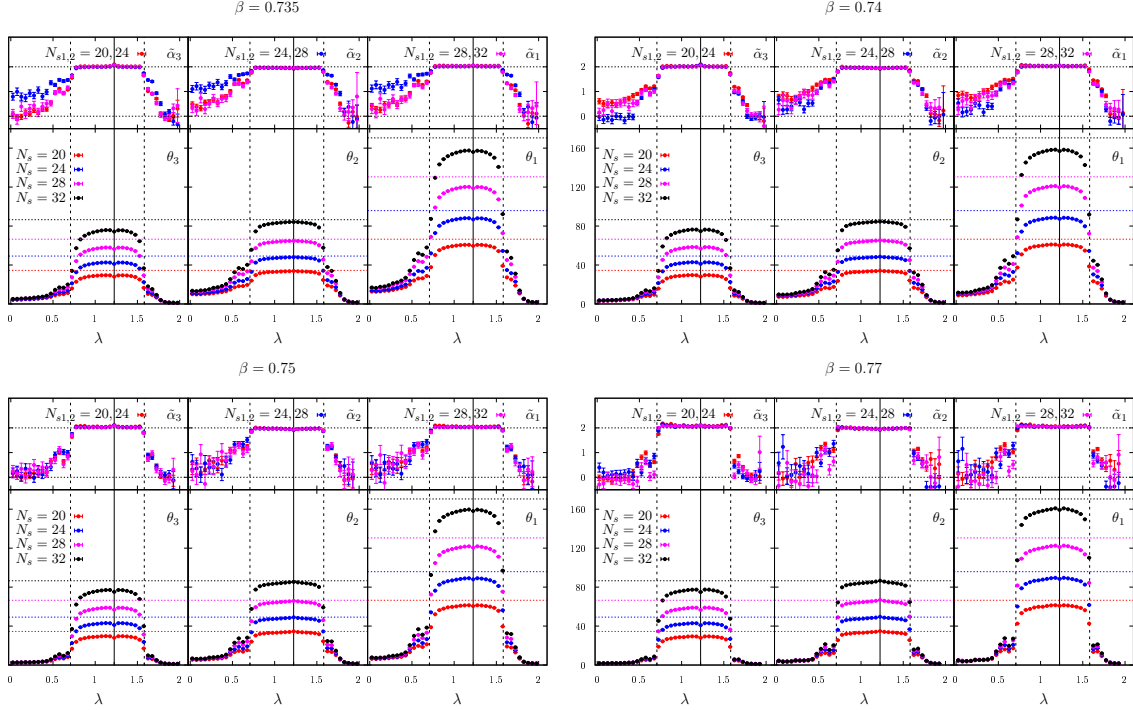


Figure 18. Bottom panels: average principal moments of inertia θ_i – deconfined phase, physical sector. The expectation for a cuboid of size $N_t \times N_s \times N_s$ is also shown (colour code matching that of the numerical data for the various volumes). Top panels: scaling dimension $\tilde{\alpha}_i$ of moment θ_i for various pairs of volumes.

In Figs. 17–20, bottom panels, we show the average principal moments of inertia θ_i of the eigenmodes, computed locally in the spectrum, for various β and spatial sizes N_s , in the physical and unphysical sectors. For comparison, we also show the theoretical expectation for a uniform $N_t \times N_s \times N_s$ cuboid extended throughout the lattice. In the top panels we show the corresponding scaling dimension $\tilde{\alpha}_i$. The shape of the modes is shown in Figs. 21 and 22. For the bulk modes, the hierarchy and the volume scaling of θ_i are approximately consistent with those of an extended cuboid in both phases and in both centre sectors. The deviations from the theoretical expectation clearly visible in θ_1 and θ_3 probably reflect the inhomogeneities in the modes due to the tendency to prefer positive Polyakov loops (see Figs. 11 and 12) and avoid negative plaquettes (see Figs. 13 and 14). Nonetheless, it seems clear that these modes are slab-like and scale like N_s in the spatial directions.

For the low modes there are clear differences between the two phases and the two sectors. Far below β_c , the shape of the lowest modes is that of a generic cuboid with a clear separation between all the principal moments of inertia, and a slight tendency to prolateness (resp. oblateness) in the physical (resp. unphysical) sector. Moving up in the spectrum, modes become more and more oblate (slab-like) in both sectors. As β_c is approached, in the physical sector all the low modes become markedly prolate, while in the unphysical sector they become

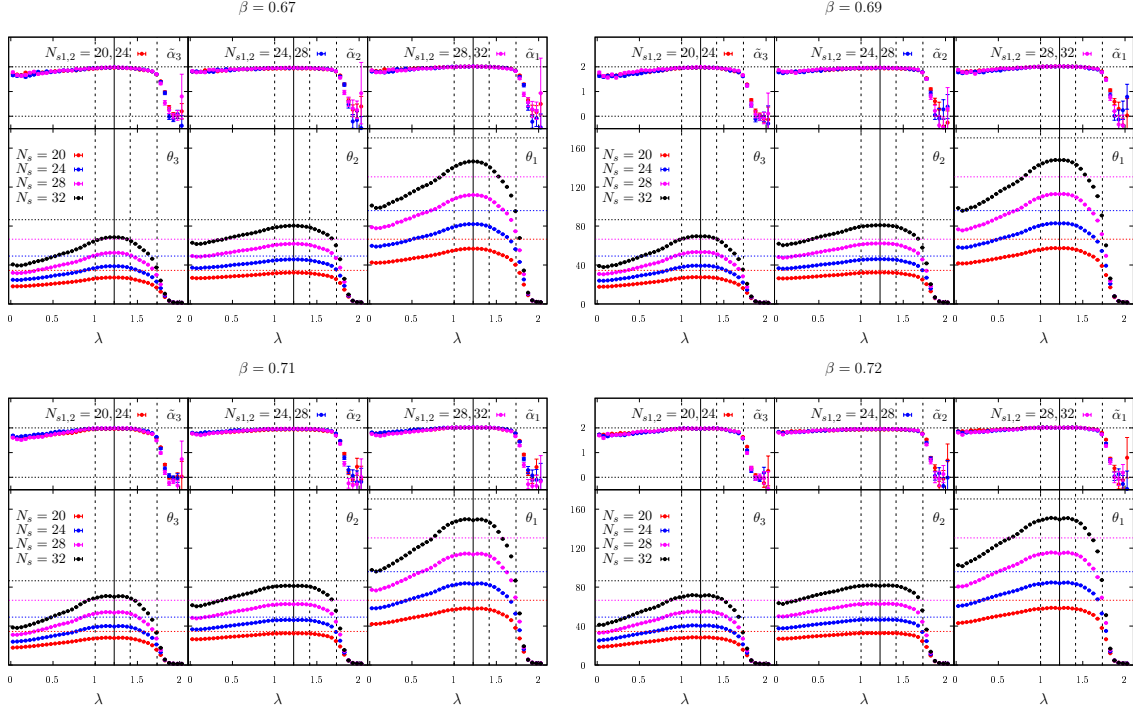


Figure 19. Bottom panels: average principal moments of inertia θ_i – confined phase, unphysical sector. The expectation for a cuboid of size $N_t \times N_s \times N_s$ is also shown (colour code matching that of the numerical data for the various volumes). Top panels: scaling dimension $\tilde{\alpha}_i$ of moment θ_i for various pairs of volumes.

markedly oblate. The volume scaling is also different below and above β_c : while in the confined phase one finds $\tilde{\alpha}_i$ only slightly below 2, in the deconfined phase the deviations from 2 become larger in the physical sector, with $\tilde{\alpha}_i$ close to zero for the lowest modes; and instead disappear in the unphysical sector. These findings are consistent with modes becoming localised, rod-like in the physical sector, and fully delocalised, slab-like in the unphysical sector.

Finally, the highest modes are prolate/rod-like in both sectors, above some point in the spectrum, both below and above β_c . In the unphysical sector this point is approximately at the high end $\lambda_{(3)}^{\text{PBC}}$ of the bulk and almost β -independent, while in the physical sector it is above the upper end $\lambda_{(1)}$ of the bulk region in the confined phase, but rather quickly reaches it as β is increased, and does not move anymore in the deconfined phase. One has approximately volume-independent $\theta_{1,2,3}$, indicating localisation. Furthermore, towards the high end of the spectrum modes tend to be spherical/cubic, with $\theta_1 \approx \theta_2 \approx \theta_3$.

These results are consistent with the picture obtained from the participation ratio. In addition, they distinguish between the localised modes found at the low and at the high end of the spectrum, that have different shapes: prolate spheroids/“rod-like” the former, and spheres/cubes the latter.

In Figs. 23 and 24 we show the average orientation of the principal axes with respect to

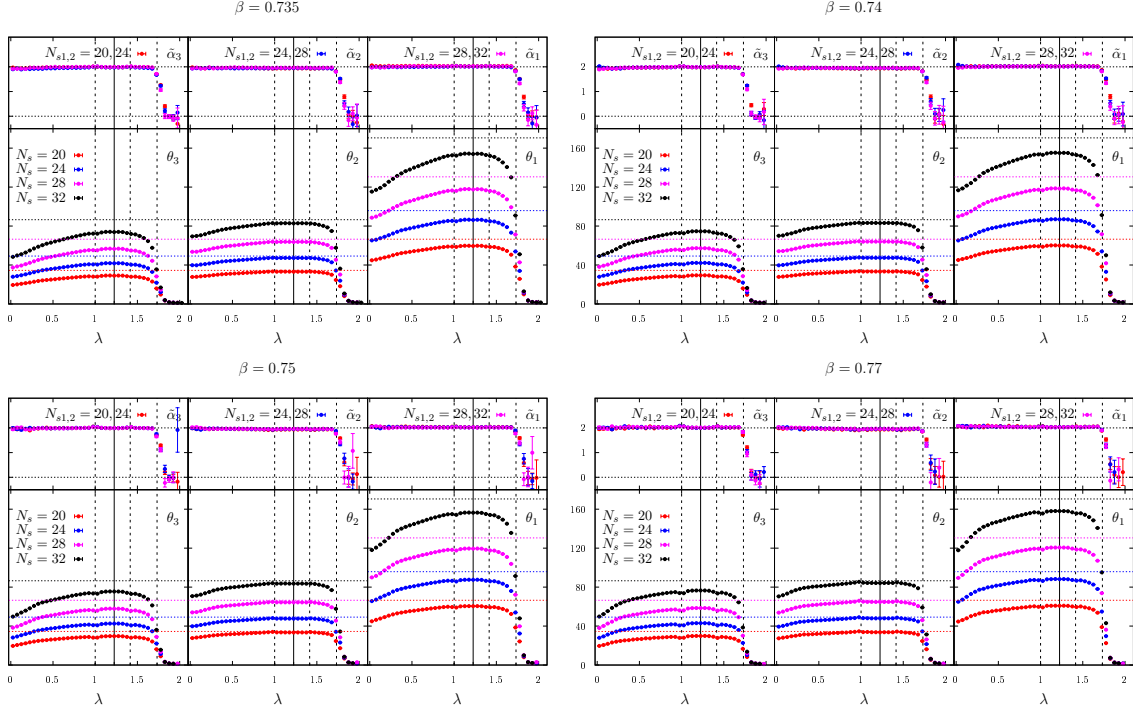


Figure 20. Bottom panels: average principal moments of inertia θ_i – deconfined phase, unphysical sector. The expectation for a cuboid of size $N_t \times N_s \times N_s$ is also shown (colour code matching that of the numerical data for the various volumes). Top panels: scaling dimension $\tilde{\alpha}_i$ of moment θ_i for various pairs of volumes.

the temporal direction (see right before Eq. (3.17)). For the largest principal moment, θ_1 , the corresponding axis is always close to the temporal direction, in all phases/sectors, and for all modes except the highest ones. Clear deviations from $\langle |\cos \varphi_1| \rangle \approx 1$ are visible in the deconfined phase in the physical sector for the low modes, and for the high modes in all phases/sectors. This reflects the fact that these modes tend to be localised not only spatially, but also in the temporal direction, albeit on a scale comparable with the temporal size (see below). In particular, for the highest modes one finds $\langle |\cos \varphi_1| \rangle \approx \frac{1}{2}$, which confirms that they have approximately spherical/cubic shape. For $\theta_{2,3}$, instead, $\langle |\cos \varphi_{2,3}| \rangle \approx 0$ in all cases and for all modes except the highest ones, with clear deviations for the low modes in the deconfined phase, and for the high modes in all phases/sectors; for the highest modes again $\langle |\cos \varphi_{2,3}| \rangle \approx \frac{1}{2}$. These results indicate that the other two principal axes prefer to lie close to the spatial plane, although sizeable fluctuations are present for the low-lying, localised modes in the physical sector of the deconfined phase. This again suggests that these localised modes are not fully extended in the temporal direction. For the spherical high modes, of course, there is no preferred direction.

Finally, in Fig. 25 we show the length scales of the equivalent cuboid for the lowest modes ($\lambda \in [0, \Delta\lambda]$) and the largest system size ($N_s = 32$). More precisely, in Fig. 25, left panel, we

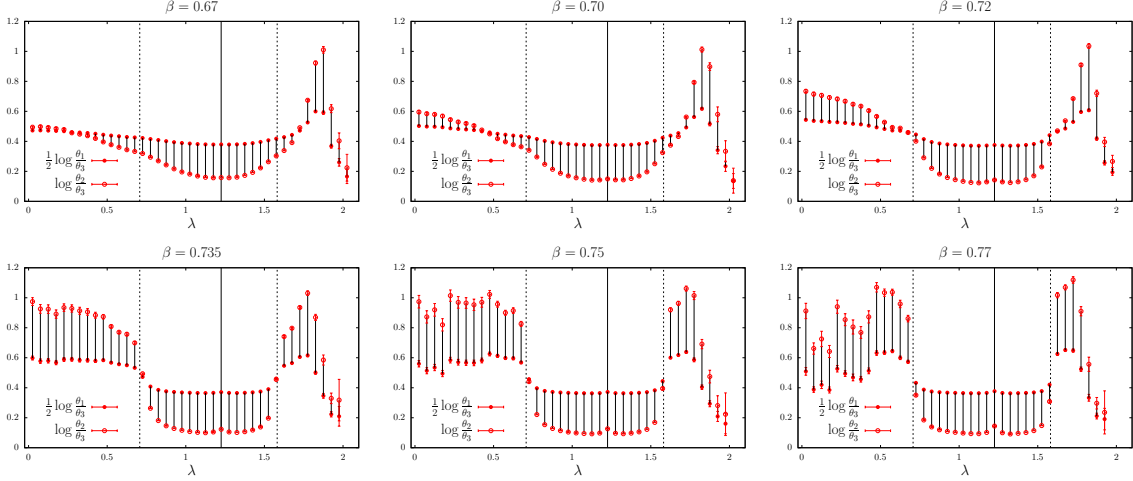


Figure 21. Shape of the eigenmodes – confined (top row) and deconfined (bottom row) phase, physical sector. Here and in the next plot, the quantity $\frac{1}{2} \log \frac{\theta_1}{\theta_3}$ measures the sphericity, and the difference $\log \frac{\theta_2}{\theta_3} - \frac{1}{2} \log \frac{\theta_1}{\theta_3} = \frac{1}{2} \log \frac{\theta_2^2}{\theta_1 \theta_3}$ measures the prolateness (if < 0) or oblateness (if > 0) of the modes. The system size is fixed to $N_s = 32$.

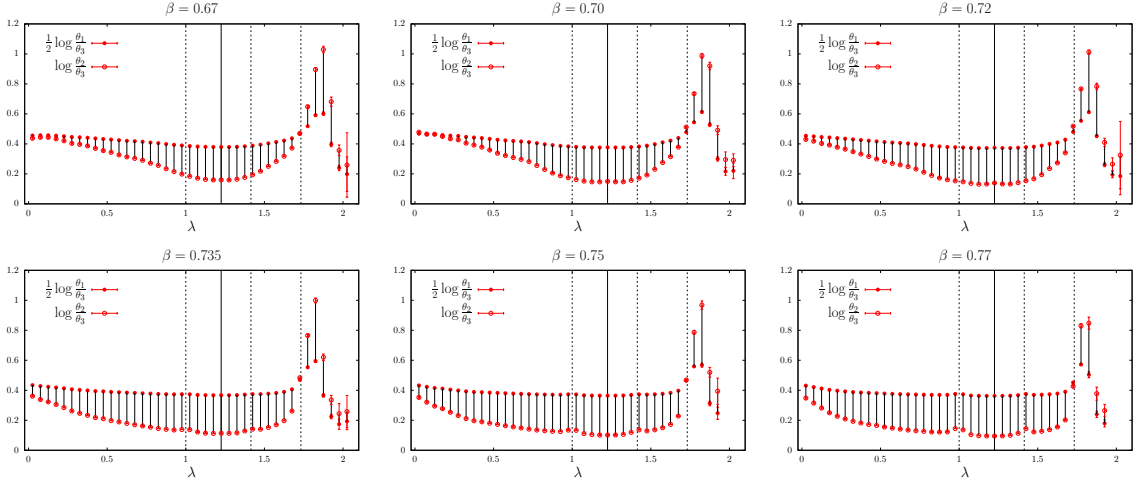


Figure 22. Shape of the eigenmodes – confined (top row) and deconfined (bottom row) phase, unphysical sector.

show the ratio $\ell_3 T / e^2 = \ell_3 \beta / N_t$, for all β s and sectors. This quantity is expected to have a finite thermodynamic limit, independently of the spatial localisation properties of the modes, as it is expected to correspond to the extension of the mode in the temporal direction. In Fig. 25, right panel, we show instead $\ell_{1,2,3} T / e^2 = \ell_{1,2,3} \beta / N_t$ in the physical sector of the deconfined phase, which are again expected to have a finite thermodynamic limit due to the localised nature of the modes. The volume dependence is indeed mild, except for $\ell_{1,2}$ closer to β_c , where finite-size effects are still important. In particular, ℓ_3 is of the same order of e^2 / T

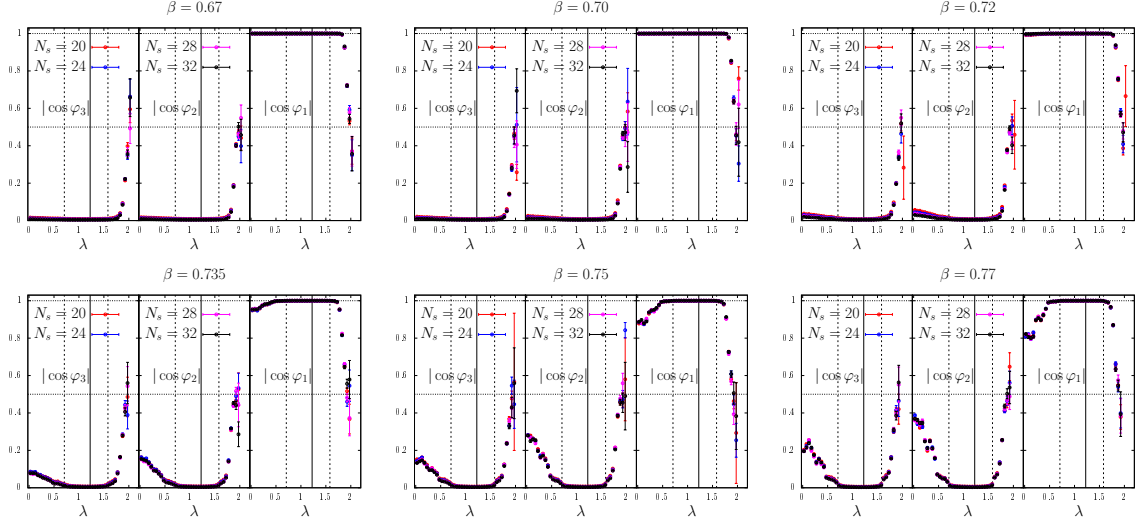


Figure 23. Average orientation of the principal axes with respect to the time direction – confined (top row) and deconfined (bottom row) phase, physical sector.

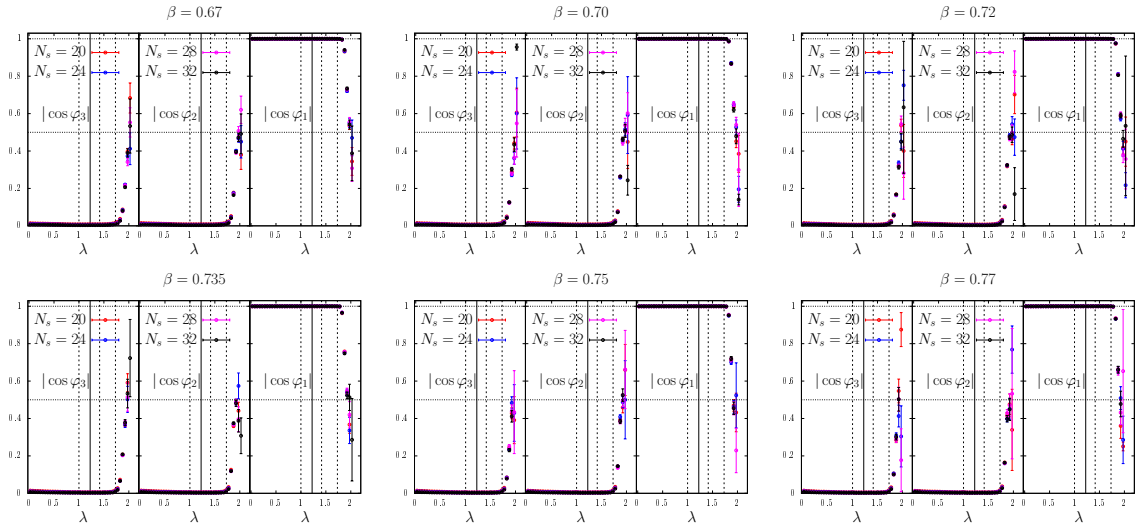


Figure 24. Average orientation of the principal axes with respect to the time direction – confined (top row) and deconfined (bottom row) phase, unphysical sector.

for all β . In the deconfined phase, in the physical (resp. unphysical) sector it becomes smaller (resp. larger) than in the confined phase, indicating a reduced (resp. increased) extension in the temporal direction. In the physical sector in the deconfined phase, all the length scales l_i are of the order of the inverse temperature.

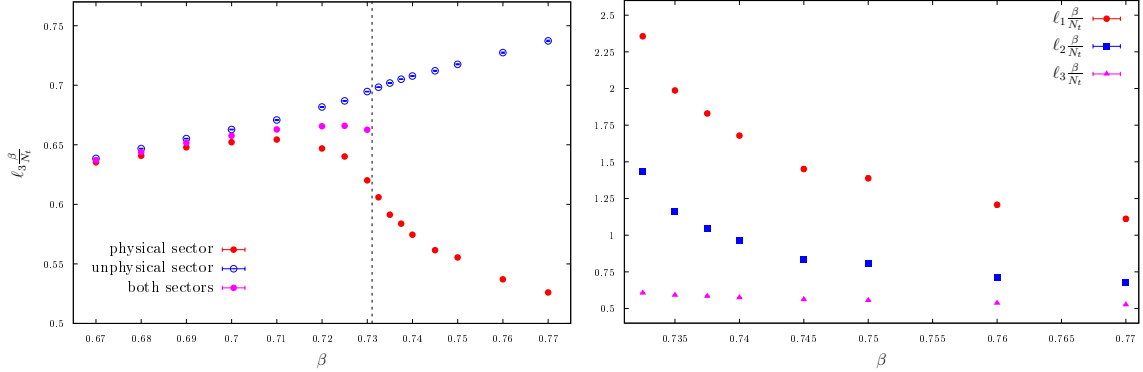


Figure 25. Left panel: temporal length scale ℓ_3 of the lowest modes in units of the inverse temperature in all phases/sectors. Right panel: length scales $\ell_{1,2,3}$ of the lowest modes in units of the inverse temperature in the deconfined phase, physical sector. $N_s = 32$ in both panels.

5 Conclusions and outlook

The finite-temperature deconfinement transition of gauge theories leads to the appearance of localised Dirac modes at the low end of the spectrum in a variety of gauge theories, both in 3+1 [6–10, 14, 16, 17, 19–21, 35] and 2+1 [18, 25] dimensions. This has been put in a relation with the ordering of the Polyakov loop in the deconfined phase, and the formation of “islands” of fluctuations in the “sea” of ordered Polyakov loops, which are expected to be the localisation centres for the low Dirac modes [15, 22, 23]. This leads one to generally expect localisation of the low Dirac eigenmodes in the high-temperature, deconfined phase of a gauge theory (in the physical centre sector).

In this paper we have studied the localisation properties of the eigenmodes of the staggered Dirac operator in the background of \mathbb{Z}_2 gauge field configurations on the lattice in 2+1 dimensions. This is the simplest gauge theory displaying a deconfining transition at finite temperature, and so provides the most basic test of the “sea/islands” picture of localisation. We have studied this theory by means of numerical simulations, producing full staggered spectra for configurations in both centre sectors in order to study in detail the effects of the ordering of the Polyakov loop, $P(\vec{x})$, throughout the whole spectrum. Our numerical results confirm the predictions of the sea/islands picture: the low-lying Dirac modes, which are delocalised in the low-temperature phase, become localised in the high-temperature phase of the theory in the “physical” centre sector, $\langle P(\vec{x}) \rangle > 0$, displaying a strong correlation with the location of negative Polyakov loops. In the “unphysical” centre sector, $\langle P(\vec{x}) \rangle < 0$, instead, the low modes remain delocalised, and show a positive correlation with the location of positive Polyakov loops. Our results suggest that localisation of the lowest modes in the physical sector takes place exactly at deconfinement, although larger a study on larger volumes is required to make a conclusive statement.

The available lattice sizes and accumulated statistics do not allow a precise determination of the mobility edge separating the low-lying, localised modes and the bulk, delocalised modes

in the deconfined phase of the theory in the physical sector. A dedicated study using larger lattices is required to determine the location of the mobility edge and understand better the nature of the corresponding Anderson transition.

A novel result obtained in this paper is that the very high modes, near the upper end of the spectrum, are localised in both phases of the theory, irrespectively of the centre sector. The localised nature of these modes can be understood similarly to that of the low modes in the physical sector at high temperature, if one recalls the “Dirac-Anderson” form of the staggered operator [23, 24]. In the Dirac-Anderson basis, the staggered operator looks like a set of N_t coupled Anderson models, with on-site “energies” provided by the phase $\phi(\vec{x}) = 0, \pi$ of the Polyakov loop along the different “branches” of the relation¹⁴ $\varepsilon_k(\vec{x}) = \sin \frac{(2k+1)\pi + \phi(\vec{x})}{N_t}$, $k = 0, \dots, N_t - 1$. Here for simplicity we take N_t to be a multiple of 4. If hopping terms are ignored, the “unperturbed” eigenstates are all spatially localised at the spatial points \vec{x} of the lattice. Moreover, when the phase of the Polyakov loop is π , two of the branches gives 0 ($k = \frac{N_t}{2} - 1$ and $k = N_t - 1$), and another two branches give ± 1 ($k = \frac{N_t}{4} - 1$ and $k = \frac{3N_t}{4} - 1$) for the on-site energy of the corresponding Anderson model. When the phase of the Polyakov loop is 0, four of the branches give $\pm \sin \frac{\pi}{N_t}$ ($k = 0, \frac{N_t}{2} - 1$ and $k = \frac{N_t}{2}, N_t - 1$), and other four of the branches give $\pm \cos \frac{\pi}{N_t}$ ($k = \frac{N_t}{4} - 1, \frac{N_t}{4}$ and $k = \frac{3N_t}{4} - 1, \frac{3N_t}{4}$). When the effect of the hopping terms is taken into account, the localised unperturbed modes mix and tend to delocalise, but they have a chance of remaining localised if they are in a spectral region where the spectral density remains sufficiently small, so that mixing is reduced. Such regions can only be outside of the spectral range of the free 2+1 dimensional Dirac operator in the two centre sectors (i.e., setting either $U_1(N_t - 1, \vec{x}) \equiv 1$ or $U_1(N_t - 1, \vec{x}) \equiv -1, \forall \vec{x}$, and all other link variables to 1). While for the spectral region near zero this is the case only at large β in the physical sector, for the high end (and its symmetric reflection in the negative spectrum) this happens in both phases of the theory. In the deconfined phase in the physical sector, the rare sites where $\phi = \pi$ are preferred by the localised modes, while in the unphysical sector only the rare sites with $\phi = 0$ can support localisation in the sea of $\phi = \pi$ sites. It would be interesting to check whether the same situation is found in physically more relevant gauge theories, e.g., in QCD.

The correlation between low modes and positive Polyakov loops observed in the unphysical sector in the deconfined phase, while not explainable in terms of “energetically” favourable islands “attracting” the mode, is not in contrast with the sea/islands picture of localisation. As pointed out in Ref. [23], an important effect of the ordering of Polyakov loops in the deconfined phase is that induces a strong correlation between different time slices, that leads to the decoupling of the Anderson models mentioned above. Conversely, the reduced correlation in the confined phase is important for their mixing, which is needed for the accumulation of low modes and the consequent spontaneous breaking of chiral symmetry. In the unphysical sector above β_c , the correlation between time slices is locally reduced where the Polyakov loop

¹⁴Here the temporal direction is taken to be direction 1, so that the corresponding staggered phase entering $\varepsilon_k(\vec{x})$ is just $\eta_1(x) = 1$.

fluctuates away from order, which in this case means that it takes the value $+1$. These locations are favourable for the different Anderson models to mix, which can lead to a lowering of the eigenvalue, and can explain the enhancement of the low modes near positive Polyakov loops.

We have also demonstrated that all localised modes display a strong correlation with the position of negative plaquettes, again in both phases of the theory and irrespectively of the centre sector. This is not entirely surprising, given the above-mentioned correlation of localised modes with Polyakov loops, and the correlation expected between Polyakov loop fluctuations and clusters of negative plaquettes. Nevertheless, the interplay between Polyakov loops, negative plaquettes, and localisation of Dirac modes certainly deserves to be studied in more detail, as it may shed light on the mechanisms of the confinement/deconfinement transition and of localisation of the low modes.

This work provides further confirmation of the close connection between localisation of the low Dirac modes and deconfinement in finite-temperature gauge theories. Given the extreme simplicity of the model, there remains little doubt concerning the universality of this connection. A possible loose end may seem the case of gauge theories that display a deconfinement transition but whose gauge group has a trivial centre, in which case the finite-temperature transition clearly cannot be associated with the spontaneous breaking of centre symmetry. Localisation of Dirac modes has not been studied yet in such theories, and so it is not clear whether it is present or not. In this case it may seem difficult to identify islands of Polyakov loop fluctuations. However, the sea/islands picture, as can be seen most easily making use of the Dirac-Anderson form of the staggered operator, favours localisation on sites where the phase of one of the eigenvalues of the Polyakov loop is close to $\pm\pi$, irrespectively of whether this corresponds to a centre element, or whether a nontrivial centre even exists at all. It may then be worth studying the \mathbb{Z}_3 gauge theory as well, where the centre is not trivial but the Polyakov loop phase cannot get closer to $\pm\pi$ than $\pm\frac{2\pi}{3}$. We hope that these kind of studies can help to shed more light on the mechanisms responsible for the deconfinement transition in finite-temperature gauge theories.

Acknowledgments

We thank T. G. Kovács for useful discussions and a careful reading of the manuscript. MG was partially supported by the NKFIH grant KKP-126769.

A Appendix: IPR for degenerate eigenspaces

Suppose to have an n -fold degenerate eigenvalue of some Hermitian Hamiltonian H , describing a system living on a finite lattice, and let $\{\psi_1(x), \dots, \psi_n(x)\}$ be an orthonormal basis of the corresponding eigenspace, with x denoting the lattice sites. It is easy to see that the IPR, $\text{IPR} = \sum_x |\psi(x)|^4$, is not constant over the vectors of unit norm, $\sum_x |\psi(x)|^2 = 1$, belonging to this eigenspace. Since no such vector is *a priori* singled out, it seems more appropriate to

assign an average IPR to the whole eigenspace by averaging over all possible vectors of unit norm. The most general such vector can be obtained as a linear combination of basis vectors as $\psi_a^U(x) = \sum_{i=1}^n U_{ai} \psi_i(x)$, where U_{ai} are the entries of a unitary $n \times n$ matrix. Here a can be fixed to any value $a = 1, \dots, n$, and it is only included for notational convenience; the final result should be independent of it. One has for the mode ψ_a^U

$$\text{IPR}_a(U) = \sum_x |\psi_a^U(x)|^4 = \sum_x \sum_{i,j,k,l=1}^n U_{ai} \psi_i(x) U_{aj}^* \psi_j(x)^* U_{ak} \psi_k(x) U_{al}^* \psi_l(x)^*. \quad (\text{A.1})$$

The average over all unit-norm vectors is obtained by group integration over U with the $U(n)$ invariant (Haar) measure, dU . To this end, we will need the following results [54],

$$\begin{aligned} \int dU U_{ij} U_{kl}^{-1} &= \text{Wg}((1), n) \delta_{il} \delta_{jk}, \\ \int dU U_{ij} U_{kl}^{-1} U_{mn} U_{pq}^{-1} &= \text{Wg}((1, 1), n) (\delta_{il} \delta_{jk} \delta_{mq} \delta_{np} + \delta_{iq} \delta_{jp} \delta_{ml} \delta_{nk}) \\ &\quad + \text{Wg}((2), n) (\delta_{il} \delta_{jp} \delta_{mq} \delta_{nk} + \delta_{iq} \delta_{jk} \delta_{ml} \delta_{np}), \end{aligned} \quad (\text{A.2})$$

where $\text{Wg}(\cdot, n)$ is the Weingarten function for the unitary group, and

$$\text{Wg}((1), n) = \frac{1}{n}, \quad \text{Wg}((1, 1), n) = \frac{1}{n^2 - 1}, \quad \text{Wg}((2), n) = -\frac{1}{n(n^2 - 1)}. \quad (\text{A.3})$$

It is now straightforward to obtain

$$\begin{aligned} \int dU \text{IPR}_a(U) &= \sum_x \sum_{i,j,k,l=1}^n \psi_i(x) \psi_j(x)^* \psi_k(x) \psi_l(x)^* \int dU U_{ai} U_{ja}^\dagger U_{ak} U_{la}^\dagger \\ &= \sum_x \sum_{i,j,k,l=1}^n \psi_i(x) \psi_j(x)^* \psi_k(x) \psi_l(x)^* \\ &\quad \times \left[\frac{1}{n^2 - 1} (\delta_{ij} \delta_{kl} + \delta_{il} \delta_{jk}) - \frac{1}{n(n^2 - 1)} (\delta_{il} \delta_{kj} + \delta_{ij} \delta_{kl}) \right] \\ &= \sum_x \left(\sum_i |\psi_i(x)|^2 \right)^2 \left(\frac{1}{n^2 - 1} - \frac{1}{n(n^2 - 1)} \right) \\ &= \frac{2}{n(n+1)} \sum_x \left(\sum_i |\psi_i(x)|^2 \right)^2. \end{aligned} \quad (\text{A.4})$$

This is independent of a , and manifestly invariant under a unitary change of basis, as it should be: indeed, $\sum_{i=1}^n |\psi_i(x)|^2 = E(x, x)$ equals the diagonal element of the projector $E(x, y)$ over the degenerate eigenspace.

It is useful to notice that for quantities of the form

$$O_i = \sum_x O(x) |\psi_i(x)|^2 \quad (\text{A.5})$$

it is sufficient to average the observables over a set of basis vectors for any orthonormal basis to automatically obtain the average of the observable over the whole degenerate eigenspace. In fact, setting

$$O_a(U) = \sum_x O(x) |\psi_a^U|^2 = \sum_x O(x) \sum_{i,j=1}^n U_{ai} U_{aj}^* \psi_i(x) \psi_j(x)^*, \quad (\text{A.6})$$

and repeating the same procedure as above, one finds

$$\begin{aligned} \int dU O_a(U) &= \sum_x O(x) \sum_{i,j=1}^n \psi_i(x) \psi_j(x)^* \int dU U_{ai} U_{aj}^* \\ &= \sum_x O(x) \sum_{i,j=1}^n \psi_i(x) \psi_j(x)^* \frac{1}{n} \delta_{ij} = \frac{1}{n} \sum_x O(x) \left(\sum_{i=1}^n |\psi_i(x)|^2 \right), \end{aligned} \quad (\text{A.7})$$

which is manifestly a - and basis-independent.

References

- [1] T. Banks and A. Casher, *Chiral symmetry breaking in confining theories*, *Nucl. Phys.* **B169** (1980) 103.
- [2] V. Dick, F. Karsch, E. Laermann, S. Mukherjee and S. Sharma, *Microscopic origin of $U_A(1)$ symmetry violation in the high temperature phase of QCD*, *Phys. Rev. D* **91** (2015) 094504 [[1502.06190](#)].
- [3] H.T. Ding, S.T. Li, S. Mukherjee, A. Tomiya, X.D. Wang and Y. Zhang, *Correlated Dirac eigenvalues and axial anomaly in chiral symmetric QCD*, *Phys. Rev. Lett.* **126** (2021) 082001 [[2010.14836](#)].
- [4] O. Kaczmarek, L. Mazur and S. Sharma, *Eigenvalue spectra of QCD and the fate of $U_A(1)$ breaking towards the chiral limit*, [2102.06136](#).
- [5] A. Patella, *A precise determination of the $\bar{\psi}\psi$ anomalous dimension in conformal gauge theories*, *Phys. Rev. D* **86** (2012) 025006 [[1204.4432](#)].
- [6] A.M. García-García and J.C. Osborn, *Chiral phase transition in lattice QCD as a metal-insulator transition*, *Phys. Rev. D* **75** (2007) 034503 [[hep-lat/0611019](#)].
- [7] T.G. Kovács and F. Pittler, *Poisson to Random Matrix Transition in the QCD Dirac Spectrum*, *Phys. Rev. D* **86** (2012) 114515 [[1208.3475](#)].
- [8] M. Giordano, T.G. Kovács and F. Pittler, *Universality and the QCD Anderson Transition*, *Phys. Rev. Lett.* **112** (2014) 102002 [[1312.1179](#)].
- [9] G. Cossu and S. Hashimoto, *Anderson Localization in high temperature QCD: background configuration properties and Dirac eigenmodes*, *J. High Energy Phys.* **06** (2016) 056 [[1604.00768](#)].
- [10] L. Holicki, E.-M. Ilgenfritz and L. von Smekal, *The Anderson transition in QCD with $N_f = 2 + 1 + 1$ twisted mass quarks: overlap analysis*, *PoS LATTICE2018* (2018) 180 [[1810.01130](#)].

- [11] M. Göckeler, P.E.L. Rakow, A. Schäfer, W. Söldner and T. Wettig, *Calorons and localization of quark eigenvectors in lattice QCD*, *Phys. Rev. Lett.* **87** (2001) 042001 [[hep-lat/0103031](#)].
- [12] C. Gattringer, M. Göckeler, P.E.L. Rakow, S. Schaefer and A. Schäfer, *A Comprehensive picture of topological excitations in finite temperature lattice QCD*, *Nucl. Phys. B* **618** (2001) 205 [[hep-lat/0105023](#)].
- [13] R.V. Gavai, S. Gupta and R. Lacaze, *Eigenvalues and Eigenvectors of the Staggered Dirac Operator at Finite Temperature*, *Phys. Rev. D* **77** (2008) 114506 [[0803.0182](#)].
- [14] T.G. Kovács and F. Pittler, *Anderson Localization in Quark-Gluon Plasma*, *Phys. Rev. Lett.* **105** (2010) 192001 [[1006.1205](#)].
- [15] F. Bruckmann, T.G. Kovács and S. Schierenberg, *Anderson localization through Polyakov loops: Lattice evidence and random matrix model*, *Phys. Rev. D* **84** (2011) 034505 [[1105.5336](#)].
- [16] M. Giordano, S.D. Katz, T.G. Kovács and F. Pittler, *Deconfinement, chiral transition and localisation in a QCD-like model*, *J. High Energy Phys.* **02** (2017) 055 [[1611.03284](#)].
- [17] T.G. Kovács and R.A. Vig, *Localization transition in $SU(3)$ gauge theory*, *Phys. Rev. D* **97** (2018) 014502 [[1706.03562](#)].
- [18] M. Giordano, *Localisation in 2+1 dimensional $SU(3)$ pure gauge theory at finite temperature*, *J. High Energy Phys.* **05** (2019) 204 [[1903.04983](#)].
- [19] R.A. Vig and T.G. Kovács, *Localization with overlap fermions*, *Phys. Rev. D* **101** (2020) 094511 [[2001.06872](#)].
- [20] C. Bonati, M. Cardinali, M. D’Elia, M. Giordano and F. Mazziotti, *Reconfinement, localization and thermal monopoles in $SU(3)$ trace-deformed Yang-Mills theory*, *Phys. Rev. D* **103** (2021) 034506 [[2012.13246](#)].
- [21] A.M. García-García and J.C. Osborn, *Chiral phase transition and Anderson localization in the Instanton Liquid Model for QCD*, *Nucl. Phys.* **A770** (2006) 141 [[hep-lat/0512025](#)].
- [22] M. Giordano, T.G. Kovács and F. Pittler, *An Ising-Anderson model of localisation in high-temperature QCD*, *J. High Energy Phys.* **04** (2015) 112 [[1502.02532](#)].
- [23] M. Giordano, T.G. Kovács and F. Pittler, *An Anderson-like model of the QCD chiral transition*, *J. High Energy Phys.* **06** (2016) 007 [[1603.09548](#)].
- [24] M. Giordano, T.G. Kovács and F. Pittler, *Localization and chiral properties near the ordering transition of an Anderson-like toy model for QCD*, *Phys. Rev. D* **95** (2017) 074503 [[1612.05059](#)].
- [25] F. Bruckmann and J. Wellenhofer, *Anderson localization in sigma models*, *EPJ Web Conf.* **175** (2018) 07005 [[1710.05662](#)].
- [26] P.W. Anderson, *Absence of Diffusion in Certain Random Lattices*, *Phys. Rev.* **109** (1958) 1492.
- [27] D.J. Thouless, *Electrons in disordered systems and the theory of localization*, *Phys. Rep.* **13** (1974) 93.
- [28] P.A. Lee and T.V. Ramakrishnan, *Disordered electronic systems*, *Rev. Mod. Phys.* **57** (1985) 287.
- [29] F. Evers and A.D. Mirlin, *Anderson transitions*, *Rev. Mod. Phys.* **80** (2008) 1355 [[0707.4378](#)].

- [30] E. Abrahams, ed., *50 Years of Anderson Localization*, World Scientific, Singapore (2010).
- [31] S.M. Nishigaki, M. Giordano, T.G. Kovács and F. Pittler, *Critical statistics at the mobility edge of QCD Dirac spectra*, *PoS LATTICE2013* (2014) 018 [[1312.3286](#)].
- [32] L. Ujjfalusi, M. Giordano, F. Pittler, T.G. Kovács and I. Varga, *Anderson transition and multifractals in the spectrum of the Dirac operator of Quantum Chromodynamics at high temperature*, *Phys. Rev. D* **92** (2015) 094513 [[1507.02162](#)].
- [33] T. Takaishi, K. Sakakibara, I. Ichinose and T. Matsui, *Localization and delocalization of fermions in a background of correlated spins*, *Phys. Rev. B* **98** (2018) 184204 [[1808.03419](#)].
- [34] A.M. García-García and E. Cuevas, *Anderson transition in systems with chiral symmetry*, *Phys. Rev. B* **74** (2006) 113101 [[cond-mat/0602331](#)].
- [35] T.G. Kovács, *Absence of correlations in the QCD Dirac spectrum at high temperature*, *Phys. Rev. Lett.* **104** (2010) 031601 [[0906.5373](#)].
- [36] F.J. Wegner, *Duality in Generalized Ising Models and Phase Transitions Without Local Order Parameters*, *J. Math. Phys.* **12** (1971) 2259.
- [37] R. Balian, J.M. Drouffe and C. Itzykson, *Gauge Fields on a Lattice. 2. Gauge Invariant Ising Model*, *Phys. Rev. D* **11** (1975) 2098.
- [38] J.B. Kogut, *An Introduction to Lattice Gauge Theory and Spin Systems*, *Rev. Mod. Phys.* **51** (1979) 659.
- [39] R.A. Vig and T.G. Kovács, *Ideal topological gas in the high temperature phase of $SU(3)$ gauge theory*, [2101.01498](#).
- [40] M. Caselle and M. Hasenbusch, *Deconfinement transition and dimensional crossover in the 3-D gauge Ising model*, *Nucl. Phys. B* **470** (1996) 435 [[hep-lat/9511015](#)].
- [41] D. Scheffler, C. Schmidt, D. Smith and L. von Smekal, *Chiral restoration and deconfinement in two-color QCD with two flavors of staggered quarks*, *PoS LATTICE2013* (2014) 191 [[1311.4324](#)].
- [42] C. Burden and A. Burkitt, *Lattice Fermions in Odd Dimensions*, *Europhys. Lett.* **3** (1987) 545.
- [43] E. Abrahams, P.W. Anderson, D.C. Licciardello and T.V. Ramakrishnan, *Scaling theory of localization: Absence of quantum diffusion in two dimensions*, *Phys. Rev. Lett.* **42** (1979) 673.
- [44] X.C. Xie, X.R. Wang and D.Z. Liu, *Kosterlitz-Thouless-type metal-insulator transition of a 2D electron gas in a random magnetic field*, *Phys. Rev. Lett.* **80** (1998) 3563.
- [45] E. König, P. Ostrovsky, I. Protopopov and A. Mirlin, *Metal-insulator transition in 2D random fermion systems of chiral symmetry classes*, *Phys. Rev. B* **85** (2012) 195130 [[1201.6288](#)].
- [46] K. Slevin and T. Ohtsuki, *Critical exponent for the quantum Hall transition*, *Phys. Rev. B* **80** (2009) 041304 [[0905.1163](#)].
- [47] Y.-Y. Zhang, J. Hu, B.A. Bernevig, X.R. Wang, X.C. Xie and W.M. Liu, *Localization and the Kosterlitz-Thouless transition in disordered graphene*, *Phys. Rev. Lett.* **102** (2009) 106401 [[0810.1996](#)].
- [48] M.L. Mehta, *Random matrices*, vol. 142, Elsevier, 3 ed. (2004).

- [49] J.J.M. Verbaarschot and T. Wettig, *Random matrix theory and chiral symmetry in QCD*, *Ann. Rev. Nucl. Part. Sci.* **50** (2000) 343 [[hep-ph/0003017](#)].
- [50] F. Gliozzi, M. Panero and P. Provero, *Large center vortices and confinement in 3-D Z(2) gauge theory*, *Phys. Rev. D* **66** (2002) 017501 [[hep-lat/0204030](#)].
- [51] L. Bai and D. Breen, *Calculating center of mass in an unbounded 2d environment*, *J. Graph. Tools* **13** (2008) 53.
- [52] E. Anderson, Z. Bai, C. Bischof, S. Blackford, J. Demmel, J. Dongarra et al., *LAPACK Users' Guide*, SIAM, Philadelphia (1999).
- [53] M. Giordano, *Localised Dirac eigenmodes, chiral symmetry breaking and Goldstone's theorem*, [2009.00486](#).
- [54] B. Collins, *Moments and cumulants of polynomial random variables on unitary groups, the Itzykson-Zuber integral, and free probability*, *Int. Math. Res. Not.* **2003** (2003) 953 [[math-ph/0205010](#)].